Advances in
Biomembranes and Lipid Self-Assembly

Volume 36

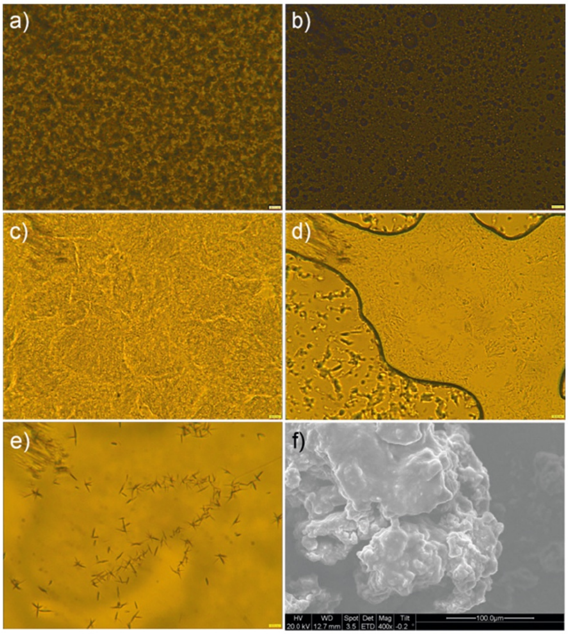

Edited by
Aleš Iglič, Michael Rappolt,
and Patricia Losada Pérez

VOLUME THIRTY SIX

ADVANCES IN BIOMEMBRANES AND LIPID SELF-ASSEMBLY

EDITORIAL BOARD

Dr. Habil. Rumiana Dimova (*Max Planck Institute of Colloids and Interfaces, Germany*)
Prof. Angelica Leitmannova Liu (*Michigan State University in East Lansing, MI, USA*)
Prof. Nir Gov (*The Weizmann Institute of Science, Israel*)
Prof. Philippe Meleard (*Ecole Nationale Superieure de Chimie de Rennes, France*)
Prof. P.B. Sunil Kumar (*Indian Institute of Technology Madras, India*)
Prof. Sylvio May (*North Dakota State University, USA*)
Prof. Thomas Heimburg (*Niels Bohr Institute, University of Copenhagen, Denmark*)
Prof. Tibor Hianik (*Comenius University, Slovakia*)
Prof. Wojciech Gozdz (*Institute of Physical Chemistry, Polish Academy of Sciences, Poland*)
Prof. Yoshinori Muto (*Gifu, Japan*)
Dr. Amin Sadeghpour (*University of Leeds, United Kingdom*)
Prof. Kazutami Sakamoto (*Chiba Institute of Science, Japan*)
Dr. Paul A. Beales (*University of Leeds, United Kingdom*)
Dr. Angelina Angelova (*Université de Paris-Sud, France*)
Dr. V.A. Raghunathan (*Raman Research Institute, India*)
Dr. Yuru Deng (*Changzhou University, China*)
Dr. Ilya Levental (*University of Virginia, USA*)
Dr. Mibel Aguilar (*Monash University, Australia*)
Dr. Chandrashekhar V. Kulkarni (*University of Central Lancashire, UK*)
Dr. Marina Inés Giannotti (*Institute for Bioengineering of Catalonia, Spain*)
Dr. Lorena Redondo-Morata (*Institute Pasteur Lille, France*)

VOLUME THIRTY SIX

ADVANCES IN BIOMEMBRANES AND LIPID SELF-ASSEMBLY

Edited by

ALEŠ IGLIČ
University of Ljubljana, Slovenia

MICHAEL RAPPOLT
University of Leeds, United Kingdom

PATRICIA LOSADA-PÉREZ
Université libre de Bruxelles, Belgium

ELSEVIER

ACADEMIC PRESS
An imprint of Elsevier

Academic Press is an imprint of Elsevier
50 Hampshire Street, 5th Floor, Cambridge, MA 02139, United States
525 B Street, Suite 1650, San Diego, CA 92101, United States
The Boulevard, Langford Lane, Kidlington, Oxford OX5 1GB, United Kingdom
125 London Wall, London, EC2Y 5AS, United Kingdom

First edition 2022

Copyright © 2022 Elsevier Inc. All rights reserved.

No part of this publication may be reproduced or transmitted in any form or by any means, electronic or mechanical, including photocopying, recording, or any information storage and retrieval system, without permission in writing from the publisher. Details on how to seek permission, further information about the Publisher's permissions policies and our arrangements with organizations such as the Copyright Clearance Center and the Copyright Licensing Agency, can be found at our website: www.elsevier.com/permissions.

This book and the individual contributions contained in it are protected under copyright by the Publisher (other than as may be noted herein).

Notices

Knowledge and best practice in this field are constantly changing. As new research and experience broaden our understanding, changes in research methods, professional practices, or medical treatment may become necessary.

Practitioners and researchers must always rely on their own experience and knowledge in evaluating and using any information, methods, compounds, or experiments described herein. In using such information or methods they should be mindful of their own safety and the safety of others, including parties for whom they have a professional responsibility.

To the fullest extent of the law, neither the Publisher nor the authors, contributors, or editors, assume any liability for any injury and/or damage to persons or property as a matter of products liability, negligence or otherwise, or from any use or operation of any methods, products, instructions, or ideas contained in the material herein.

ISBN: 978-0-323-98596-3
ISSN: 2451-9634

For information on all Academic Press publications
visit our website at https://www.elsevier.com/books-and-journals

Publisher: Zoe Kruze
Acquisition Editor: Jason Mitchell
Developmental Editor: Paulo
Production Project Manager: Abdulla Sait
Cover Designer: Miles Hitchen

Typeset by STRAIVE, India

ELSEVIER
Book Aid International
Working together
to grow libraries in
developing countries
www.elsevier.com • www.bookaid.org

Contents

Contributors

Amrutha Arimboor Sunny
Centre for Smart Materials, School of Natural Sciences, University of Central Lancashire, Preston, United Kingdom

Mitja Drab
Laboratory of Physics, Faculty of Electrical Engineering, University of Ljubljana, Ljubljana, Slovenia

Tamar Garcia-Sorribes
Centre for Smart Materials, School of Natural Sciences, University of Central Lancashire, Preston, United Kingdom

Veronika Kralj-Iglič
Laboratory of Clinical Biophysics, Chair of Orthopaedic Surgery, Faculty of Medicine; Laboratory of Clinical Biophysics, Faculty of Health Sciences, University of Ljubljana, Ljubljana, Slovenia

Chandrashekhar V. Kulkarni
Centre for Smart Materials, School of Natural Sciences, University of Central Lancashire, Preston, United Kingdom

Yogita Patil-Sen
Centre for Smart Materials, School of Natural Sciences, University of Central Lancashire, Preston, United Kingdom

Adam Squires
School of Chemistry, University of Reading, Whiteknights, Reading, United Kingdom

Sergey Zlatogorsky
Centre for Smart Materials, School of Natural Sciences, University of Central Lancashire, Preston, United Kingdom

Preface

For the 36th volume of *Advances in Biomembranes and Lipid Self-Assembly* (*ABiLSA*), we have two contributions covering diametrically opposite research fields. While once again providing stimulating reviews, each in its own right, we do believe that the way forward for the *ABiLSA* book series will be to organize topic-oriented volumes. These compilations will either provide a scientific stage for research departments, who like to review their recent research activities (see, for instance, Volume 30), or will be open to invitations around the world. Future research topics will be proposed by our editorial board, and a 5-year program decided by the editors will help populate various research topics in parallel, covering both theoretical and experimental methods as well as simulation studies.

Returning to the 36th volume, the structural and physicochemical characterization of various butter oils is presented in detail in Chapter 1. Following their hierarchal structure analysis, employing microscopic and X-ray scattering methods, their solubility, density, thermal behavior, and functional groups are also elucidated in this report. In Chapter 2, the scientific question focuses on Fermi gas and how it may mediate an attractive force between two parallel planes of equal charge. The main mechanism of energy storage remains the electric double layer, but new solutions are presented, which might be significant in biomembrane systems, in which adhesion and interaction between charged surfaces are a common scenario.

We thank all the authors who contributed to Volume 36; that is, we are grateful to Chandrashekhar V. Kulkarni and Mitja Drab and all their coauthors. We express our gratitude to Jason Mitchell from the Elsevier Office in Oxford, Cindy Angelita Pe Benito-Gardose from the Elsevier Office in Manilla, Abdulla Sait from the Elsevier Office in Chennai, and all members of the editorial board who contributed to the preparation of this volume of *ABiLSA*.

Aleš Iglič
Michael Rappolt
Patricia Losada-Pérez

CHAPTER ONE

Lipid nanostructures in butter oil: Structural and physicochemical characterization

Amrutha Arimboor Sunny[a], **Sergey Zlatogorsky**[a], **Yogita Patil-Sen**[a], **Tamar Garcia-Sorribes**[a], **Adam Squires**[b,†], and **Chandrashekhar V. Kulkarni**[a,*]
[a]Centre for Smart Materials, School of Natural Sciences, University of Central Lancashire, Preston, United Kingdom
[b]School of Chemistry, University of Reading, Whiteknights, Reading, United Kingdom
*Corresponding author: e-mail address: cvkulkarni@uclan.ac.uk

Contents

Abstract

Butter oil is derived from butter and constitutes of triglycerides along with small amounts of other lipids and fat-soluble components. Food grade lipids can be easily sourced from butter oil which finds a great potential in various ancient, modern as well as emerging applications. Due to almost “all fat” content, butter oil is not soluble in water, but it can be emulsified or combined with other components to enhance its applicability. In order to develop and optimize various applications, it is vital to identify self-assembled nanostructures formed within the butter oil. This report involves nanostructural studies by small (SAXS) and wide (WAXS) angle X-ray scattering and microstructural analysis of butter and butter oil using microscopic techniques. Both butter and butter oil display various polymorphs, detected by WAXS, but in general, the

---

[†] Current address: Department of Chemistry, University of Bath, Bath, BA2 7AY, United Kingdom.

Advances in Biomembranes and Lipid Self-Assembly, Volume 36
ISSN 2451-9634
https://doi.org/10.1016/bs.abl.2022.10.001

self-assembled nanostructure was identified to be a lamellar phase with the lattice parameter of about 41.8 Å. Physicochemical properties of butter oil, namely solubility, density, thermal behavior, functional groups and molecular structure elucidation also contribute to this report.

1. Introduction

Butter oil is, primarily, a dairy-based product that contains more than 99% lipids. It is produced by heating food-grade butter obtained by (i) fermentation (with starter cultures) followed by churning of milk cream or by (ii) churning of fresh milk cream (unfermented cream) [1,2]. Butter oil and its variants are known by various names across the globe, including *Ghrita*, ghee, *maslee*, *samn*, *roghan*, clarified butter and anhydrous milk fat (AMF) [2]. 100 g butter oil typically contains triglycerides (triacylglycerols, TAGs) as a major component (97–98 g), linoleic acid (1–2 g), phospholipids (up to 28 mg), cholesterol (178 mg), small amounts of fatty acids (of which 16:0 and 18:1 are abundant) and a few micrograms of vitamin A and vitamin E [3,4].

Interesting properties of butter oil that contribute to its applicability include long shelf life (about 6–8 months)—even at tropical temperatures [5,6], high flash point (>200 °C) [7], characteristic flavor (favored by many), ability to solubilize essential and nutritional molecules (e.g., vitamins), its own antioxidant [7] and therapeutic properties and easy availability at commercial as well as household level. Although it is a dairy-based product, the non-fat components are removed during its production, hence it is considered to be suitable for lactose and casein intolerant people [7].

Butter oil has been highly functional in preparing Ayurvedic formulations since ancient times [8,9] whereas other applications include high temperature cooking, other culinary practices (frying or garnishing of food products) and, in some parts, to perform religious rites [2]. Medical applications [7] of butter oil include wound healing, reducing inflammation, easing digestion and improving immunity. A proposed application of butter oil involves production of biodiesel by its transesterification using alkaline catalyst [10].

Being highly hydrophobic (with 99% lipids), butter oil is not miscible with water. However, it is a good carrier for hydrophobic ingredients, namely fat-soluble vitamins, essential fatty acids and nutrients [7]. An ultrasonic processing technique has been successfully employed to develop oil-in-water emulsions of butter oil, which are promising for loading various active ingredients [11]. By addition of various other ingredients, it is possible to prepare nanostructured formulations for loading hydrophilic, hydrophobic and/or amphiphilic molecules [12]. In order to optimize these formulations for efficient loading and controlled release of various active components, it is essential to know which type of lipid phases (nanostructures) are formed by pure butter oil under various conditions. Crystallization properties and chemical composition of butter oil have been widely explored [13–17], however, its morphological behavior, particularly studies on formation of lipid nanostructures, e.g. at various temperatures, have not been reported yet. Using small- and wide-angle X-ray scattering we have identified self-assembled lipid nanostructures displayed by butter and butter oil at various temperatures and hydrations. These studies are supported by selected physicochemical and thermal analyses.

2. Source of butter oil

Butter oil for this work was obtained from three different sources: (1) butter oil prepared in our laboratory, (2) ready-made butter oil (named as Cow ghee) produced by Gowardhan (Parag Milk Foods Ltd. Mumbai, India; Batch no. AGHE22F02A) and (3) ready butter oil (named as Desi Ghee) produced by Anwar (UK) Ltd., Glasgow, UK (obtained in July 2022). Butter used for X-ray scattering and thermal studies was obtained from Lurpak, UK (Batch no. 2091). All products were stored in fridge (at about 4 °C) prior to their analyses.

Butter oil was prepared from commercial unsalted butter (Cowbelle, Aldi Stores Ltd. UK or Lurpak, UK) using a method reported in Reference [11] (Fig. 1). Briefly, an unsalted butter (Batch no. 51012279) was melted at about 70 °C followed by heating above 100 °C to evaporate moisture and convert butter into a butter oil. Heating was reduced again to 70 °C and stopped completely when solids transform into a brown residue (Fig. 1) [18]. The latter was filtered and treated with hexane to separate the butter oil (lipid content). The liquid portion (butter oil) was golden in color and had a pleasant smell, characteristic of Maillard reactions [19] in dairy products, signifying that the butter oil was ready. Gravimetric estimation of the composition of the butter was as follows: butter oil 81.9%, moisture 14.9% and brown residue 3.2%, which were close to the literature values [20,21] (Fig. 1). As mentioned earlier, butter oil is composed of >99% lipids. The brown residue is formed by condensation of milk proteins and/or amino acids and carbohydrates; the reaction is called Maillard reaction, discovered by Maillard in 1912 [22].

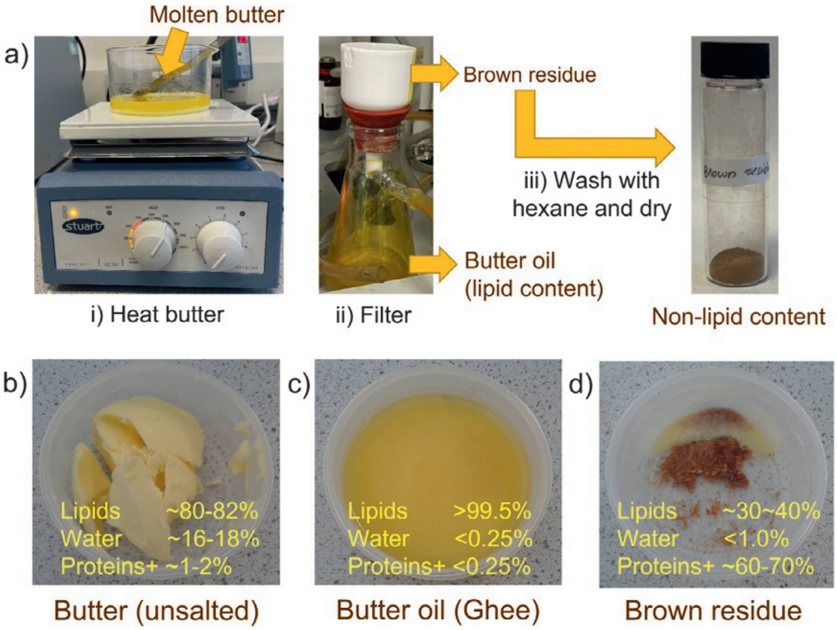

Fig. 1 (A) Preparation of butter oil from unsalted butter and approximate compositions of (B) butter, (C) butter oil and (D) brown residue. Data for butter and butter oil was obtained from *USDA, National Nutrient Database for Standard Reference Release 27* [20,21]. Hexane-treatment removed lipid-content from the brown residue (non-lipid content, primarily composed of dairy proteins and carbohydrates [1], was estimated taking mass balance into account).

3. Lipid nanostructures and polymorphism in butter oil

Butter oil is mainly composed of triglycerides (lipids). Lipids contain both hydrophilic and hydrophobic parts within the same molecule, which facilitates their self-assembly into various phases—nanostructured polymorphs. Dairy products, containing triglycerides, usually form lamellar (fluid L_α, gel L_β or crystalline L_C) and fluid isotropic (L_2) phases [23,24]. Small and wide-angle X-ray scattering (SAXS/WAXS) experiments were performed to determine the nanostructural properties of butter oil. Bruker analytical X-ray system with Bruker SAXS data collection and analysis software were used for this work. Small angle X-ray scattering (SAXS) studies on butter and butter oil confirm the presence of lamellar phases at 20 °C (Fig. 2A); first two order peaks are clearly visible (indicated by Bragg's peak ratios 1, 2). Lattice parameters of both butter (41.5 Å) and butter oil (41.8 Å) were similar at room temperature (20 °C). Fluid lamellar phase (L_α) typified by broad peak around 4.5 Å is present in both butter

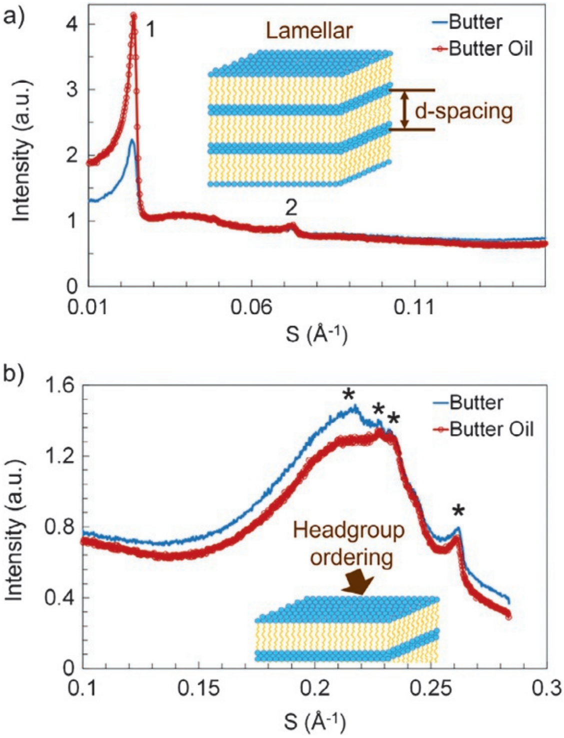

Fig. 2 (A) Small and (B) wide angle X-ray scattering patterns of butter and butter oil at 25 °C. Bragg's peak ratios designated by numbers 1 and 2 (in SAXS) represent lamellar phase. Peaks shown by * sign (in WAXS) reveal lamellar crystalline polymorph (L_C) whereas broad peak (in WAXS) reports presence of fluid lamellar polymorph (L_α). Schematic drawings portray three-dimensional structure of a lamellar phase.

and butter oil; however, the crystalline polymorphs (L_C) slightly differ: in case of butter L_C has four peaks at lattice spacing of 4.6 Å, 4.4 Å, 4.3 Å and 3.8 Å whereas butter oil does not show peak at 4.6 Å (Fig. 2B). SAXS usually provides information about repeating patterns along z-axis (in lamellar phase) i.e. d-spacing (lattice parameter) while WAXS is useful to distinguish polymorphism in lamellar phases as lipid headgroups exhibit distinct ordering along the x-y plane.

Triglycerides are known to exhibit wide-range of polymorphism as reported earlier through detailed XRD analyses [25]. Lattice spacings seen in our WAXS analysis (within an error of ±0.2 Å) confirm the presence of such polymorphism [25]: a characteristic short spacing at 4.6 Å represents the most stable β polymorph which has a triclinic subcell; the β′ form with characteristic spacings at 3.8 Å and 4.2 Å has an orthorhombic subcell structure.

Peak broadening (in SAXS) is typically observed as the temperature increases, which is attributed to a decrease in ordering within a sample and/or increase in its fluidity (Fig. 3). At 37 °C, there is a detectable peak for butter, but it is not visible for butter oil as it is almost completely molten at this temperature. The lattice parameter of lamellar nanostructure found to increase with temperature (Table 1), as closely packed (frozen)

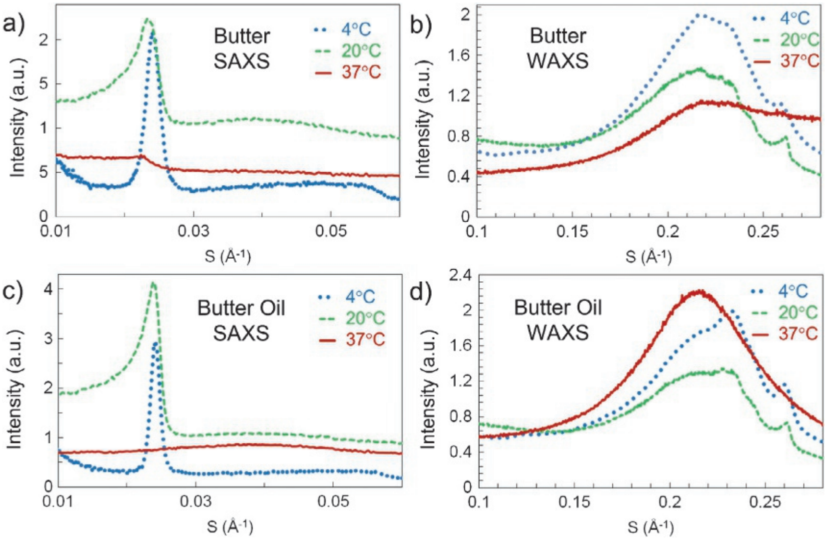

Fig. 3 Small (A) and (C) and wide (B) and (D) angle X-ray scattering patterns of butter and butter oil at various temperatures.

Table 1 Lattice parameters of lamellar nanostructure determined by SAXS at various temperature (4 °C—storage temperature, 20 °C/25 °C—room temperature and 37 °C—physiological temperature).

Sample	**Temperature (°C)**	**Lattice parameter (Å)**
Butter	4	41.2
Butter	20	41.5
Butter	25	41.8
Butter	37	43.9
Butter oil	4	41.3
Butter oil	20	41.8
Butter oil	25	42.1
Butter oil	37	No peak

bilayers at low temperatures become fluid enough to straighten themselves thereby causing their thickening.

In WAXS patterns (Fig. 3), crystalline lamellar L_C polymorphs were evident at 4 °C and 20 °C with coexisting fluid lamellar L_α (typical broad peak around 4.5 Å) but at 37 °C only fluid lamellar phase was retained. The latter is a true liquid crystalline phase observed in lipid systems.

Butter and butter oil are largely hydrophobic as they primarily consist of triglycerides [4,21]. They are also not soluble in water. However, they show slight change in scattering patterns when mixed with excess water as confirmed through SAXS/WAXS studies at room temperature, 25 °C (Fig. 4).

Upon addition of water, the lattice parameter for butter increased slightly (from 41.8 Å to 42.9 Å), whereas for butter oil there was no detectable change (42.1 Å). In case of brown residue there was a little decrease in lattice parameter when mixed with water (from 42.1 Å to 41.8 Å). Nonetheless, the changes are insignificant (error in determination of lattice parameter by SAXS is ±0.5 Å). A little change in butter and brown residue could be attributed to the interaction of water molecules with hydrophilic content (e.g. carbohydrates and proteins) in them [1,21].

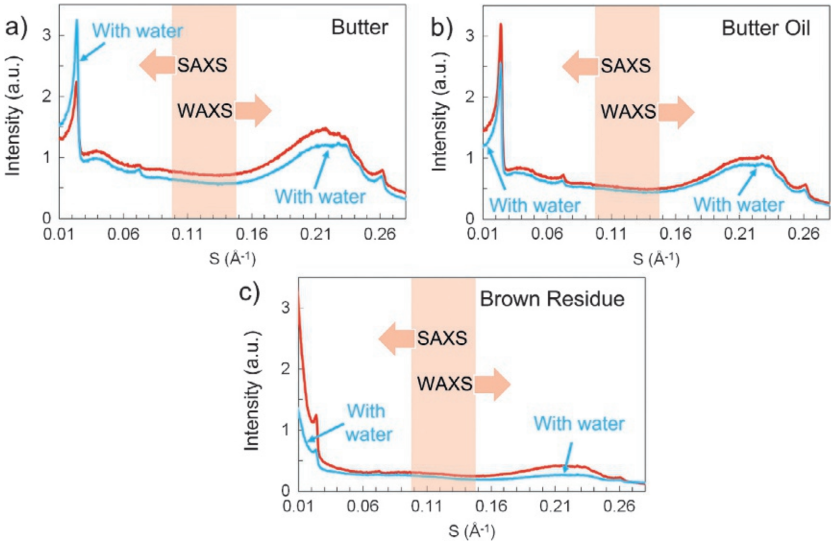

Fig. 4 Small and wide-angle X-ray scattering patterns of butter, butter oil and brown residue at 25 °C.

4. Microscale morphology of butter oil

Nanoscale morphology of butter and butter oil was studied using X-ray scattering technique whereas microstructure was observed under optical microscope and scanning electron microscopy (SEM) at room temperature. Novex (Holland) microscope attached to CMEX 1300x camera was utilized to obtain optical micrographs of various samples at room temperature, which were analyzed using Image-Focus software. Scanning electron microscopy (SEM) was conducted on brown residue after gold sputtering for 35 s. Butter shows dense packing (Fig. 5A) of its constituents

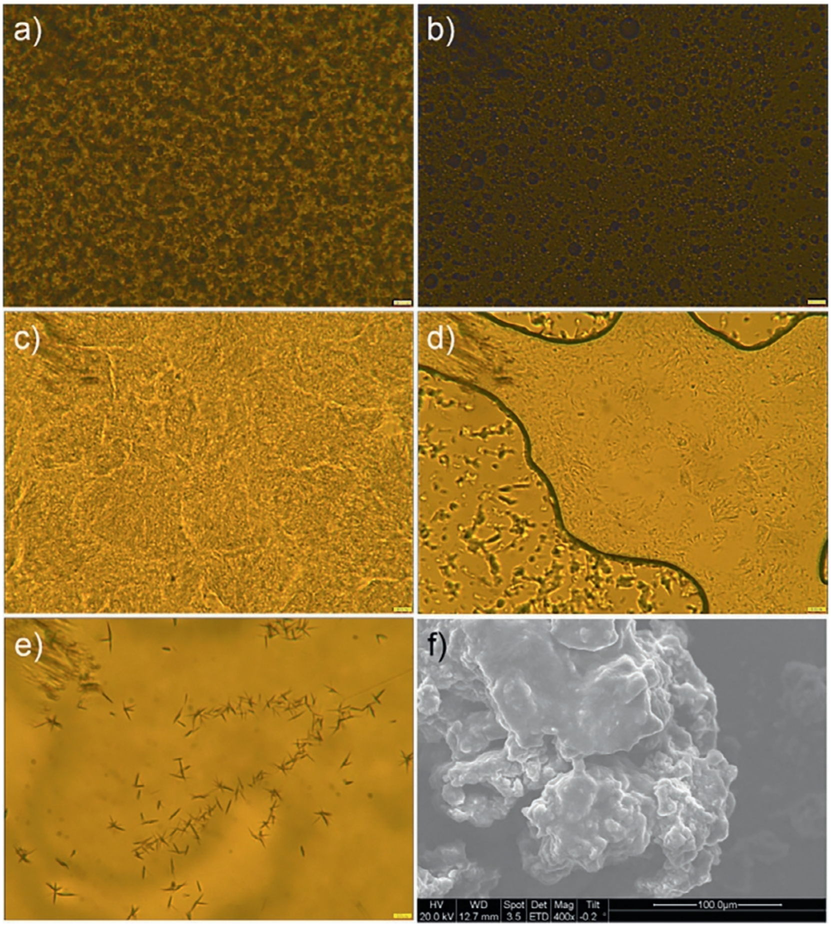

Fig. 5 Optical micrographs of butter (A) and (B) and butter oil (C), (D) and (E). (F) SEM image of brown residue (before hexane wash). Scale bar in all images indicate 100 µm.

along with some water and/or lipid droplets of two different populations (Fig. 5B): (i) non-transparent solid droplets, sizes less than 10 μm and (ii) transparent droplets, sizes in the range of 10–80 μm.

Butter oil, on the other hand, contains lipids as abundant constituents and displays a different texture (Fig. 5C). This texture, however, changes when the sample was left on the microscope slide for about 10 min; molten lipid from butter oil sample is noticeable in Fig. 5D. Upon 5 min of cooling in the fridge, needle-like microcrystals (size ~20–80 μm) appeared, which tend to aggregate into larger structures (size ~100–150 μm) as evident in Fig. 5E. Such hierarchically organized morphology is commonly seen in case of dairy lipids [25], particularly the triacylglycerols (TAGs). SEM picture of brown residue shows solid-like architecture (Fig. 5F), but it appears more to be amorphous rather than crystalline structure. Hexane washing transformed this sticky mass into free-flowing powder (Fig. 1).

5. Spectroscopic characterization of butter oil

IR and NMR spectroscopies were used to elucidate the structure of the main component of butter oil. Presence of various functional groups in the butter and butter oil was determined using Thermo Scientific Nicolet IR 200 Fourier Transform Infra-Red (FTIR) Spectrometer with the ATR attachment at room temperature against the air background. Nuclear magnetic resonance (NMR) spectra were recorded on a Bruker Avance II$^+$ spectrometer operating at 400 MHz for ^{1}H and 100 MHz for ^{13}C. Spectra were recorded for molten butter oil at 50 °C using flame sealed $(CD_3)_2SO$ capillaries for lock.

Both butter and butter oil show the prominent C=O stretch at 1743 cm^{-1}, C—H stretching peaks at 2922 and 2852 cm^{-1}, C—O stretching at 1159 cm^{-1} and very similar fingerprint region, which is expected as butter contains 81.9% of butter oil (Fig. 6). This clearly indicates the presence of the ester groups (from triglyceride) [26].

As the brown residue only comprises 3.2% of butter, and it is the product of the heat treatment of butter which is associated with chemical changes [19], the peaks detectable in the IR spectrum of the brown residue will not necessarily be present in the spectrum of butter.

In the IR spectrum of brown residue, there is the broad OH stretch centered at 3284 cm^{-1} which overlaps with the N—H stretches at 3521, 3373, 3334 and 3265 cm^{-1}, which is consistent with the presence of carbohydrates and proteins (Fig. 6). The C=O stretch is essentially absent, meaning that the majority of triglycerides were removed.

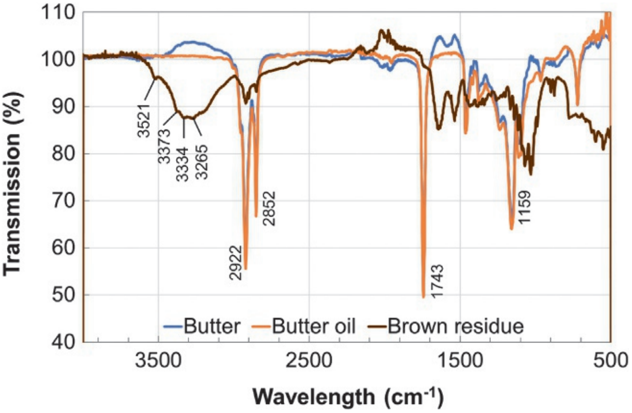

Fig. 6 FTIR spectra of butter, butter oil and brown residue.

^{1}H, ^{13}C{^{1}H}, DEPT135 and a range of 2D NMR spectroscopic methods were used to determine the structure of the main component of butter oil. The spectra were recorded for molten butter oil in the absence of any solvents, to exclude potential intermolecular interactions between the components of the butter oil and solvent molecules. To ensure spectra are resolved at the level required for interpretation these were recorded at 50 °C, which is the temperature at which the fluidity of the butter oil is high enough to obtain satisfactorily resolved spectra.

We found the two major components in the analyzed sample of butter oil, the triglyceride and the unsymmetrical alkene $RCH_2CH{=}CHCH_2R'$ (Fig. 7), in a 1:0.585 molar ratio, according to NMR integration. Throughout all NMR spectra (Figs. 7–13), hydrogen and carbon atoms of the triglyceride are referred to as color coded Latin letters **c** to **h** and **A**, **C—H** (**small blue** for ^{1}H and **CAPITAL GREEN** for ^{13}C); and for the identifiable fragments of the alkene as color coded Greek letters $\boldsymbol{\delta}$, $\boldsymbol{\gamma}$ and $\boldsymbol{\pi}$, and $\boldsymbol{\Delta}$, $\boldsymbol{\Gamma}$ and $\boldsymbol{\Pi}$, respectively (Figs. 7 and 8); please note that the color coding is not used in the text. Detailed assignment of all unambiguous peaks for all NMR methods used is presented in Table 2.

For the unsymmetrical alkene $RCH_2CH{=}CHCH_2R'$, the multiplet between 5.02 and 4.94 ppm in ^{1}H NMR spectrum (Fig. 7) is assigned to two protons at the double bond, $\mathbf{H_\delta}$-C=C-$\mathbf{H_\gamma}$. This multiplet is represented by two overlapping doublets of triplets (expected for the fragment $RCH_2CH{=}CHCH_2R'$) with the overall width of approx. 26 Hz, which most probably indicates *cis* isomer [27]: typical $^3J_{cis} = 12\,Hz + 2x$(typical $^3J = 7\,Hz) = 26\,Hz$ in an assumption that the chemical shifts for $\mathbf{H_\delta}$ and

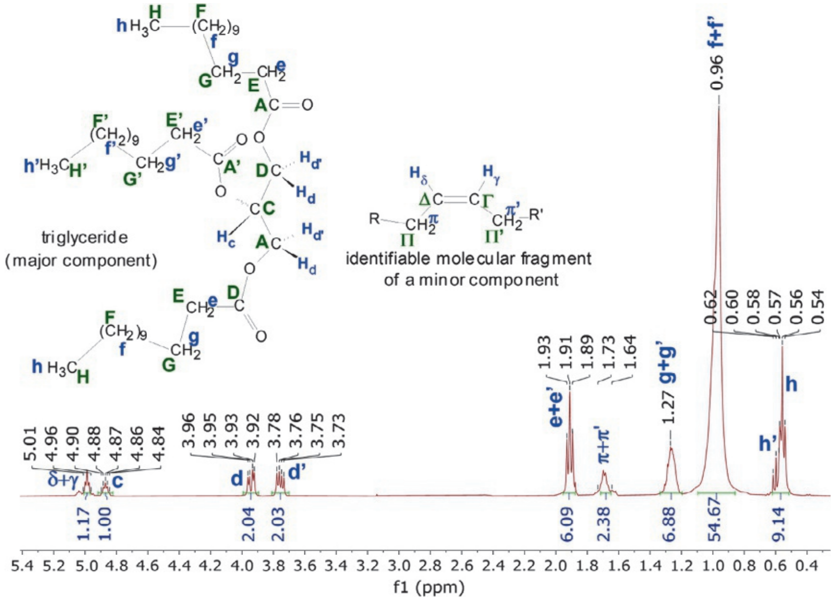

Fig. 7 ^{1}H NMR (400 MHz, 50 °C, $(CD_3)_2SO$ capillary for lock) of butter oil and annotated molecular structures of major components.

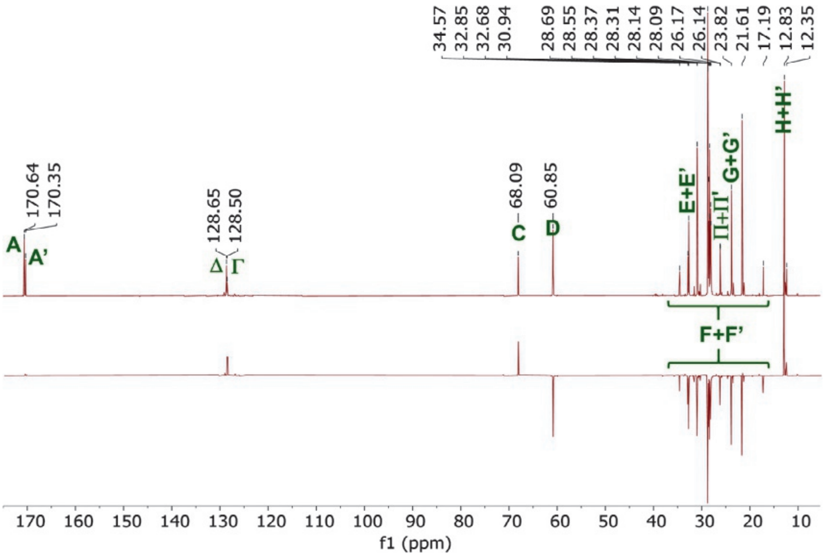

Fig. 8 $^{13}C\{^{1}H\}$ (top trace) and DEPT135 (bottom trace) NMR (100 MHz, 50 °C, $(CD_3)_2SO$ capillary for lock) of butter oil.

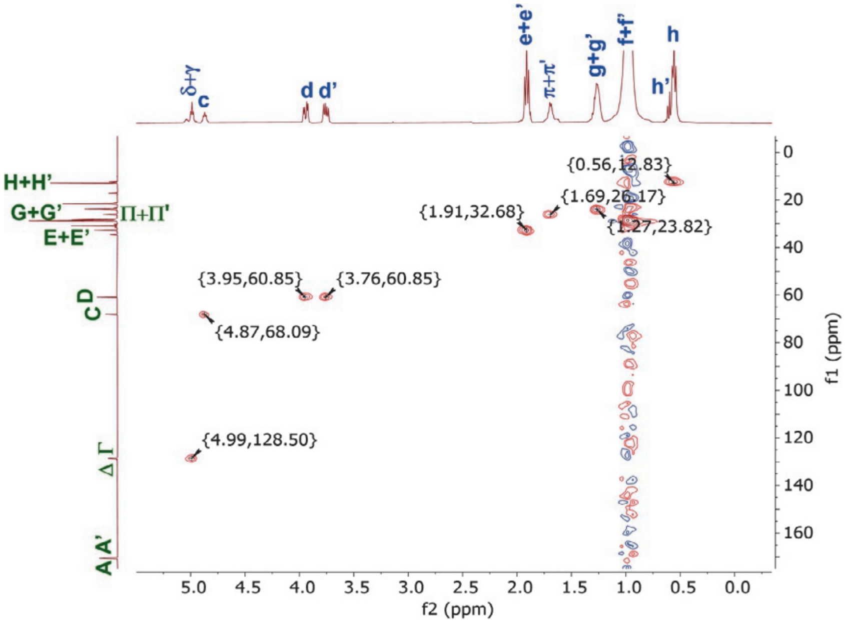

Fig. 9 ^{1}H-^{13}C HSQC NMR (50 °C, $(CD_3)_2SO$ capillary for lock) of butter oil.

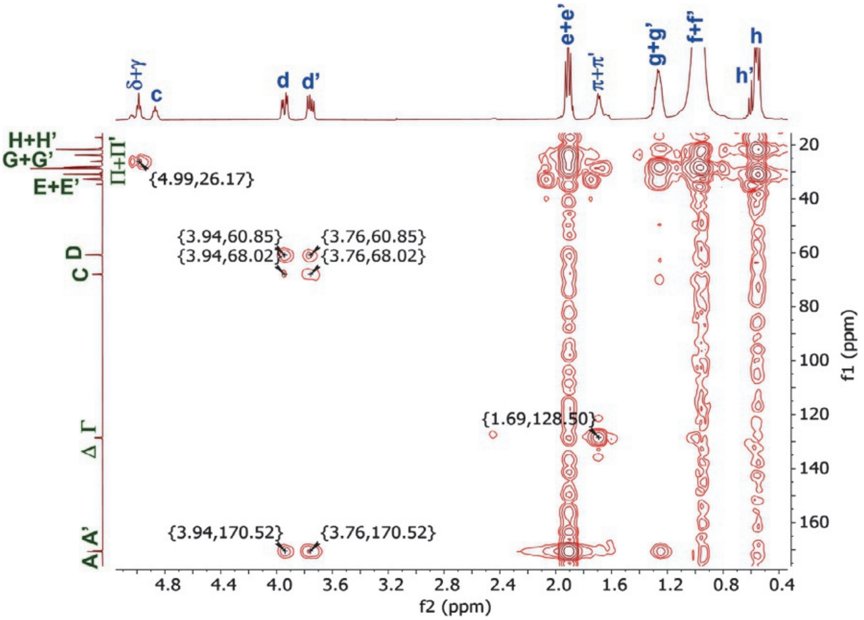

Fig. 10 ^{1}H-^{13}C HMBC NMR (50 °C, $(CD_3)_2SO$ capillary for lock) of butter oil.

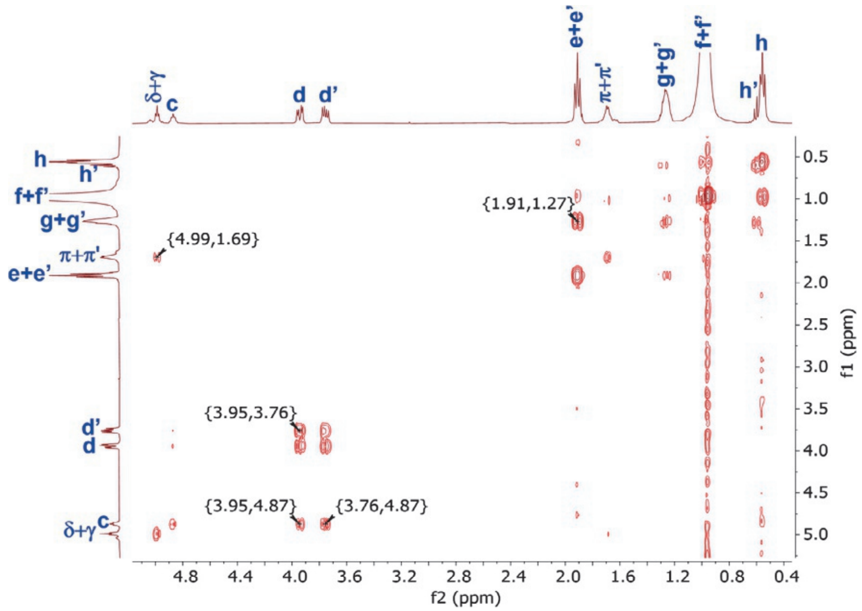

Fig. 11 ^{1}H-^{1}H COSY NMR (50 °C, $(CD_3)_2SO$ capillary for lock) of butter oil.

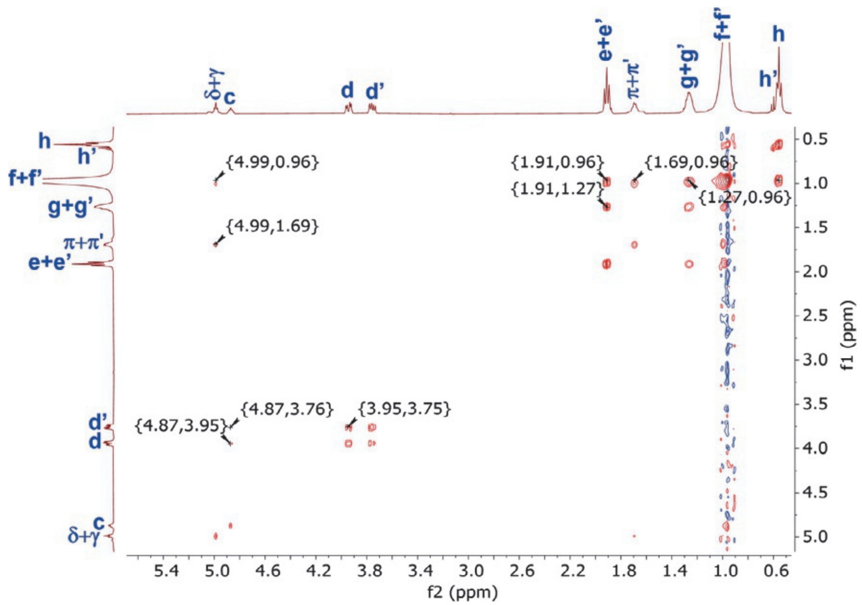

Fig. 12 ^{1}H-^{1}H TOCSY NMR (50 °C, $(CD_3)_2SO$ capillary for lock) of butter oil.

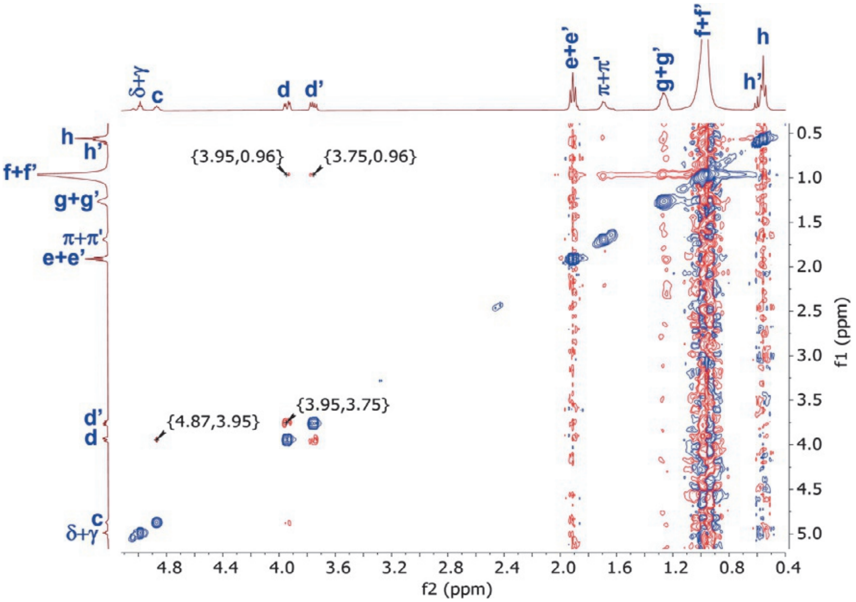

Fig. 13 ^1H-^1H ROESY NMR (50 °C, $(CD_3)_2SO$ capillary for lock) of butter oil.

$\mathbf{H_\gamma}$ are the same (larger dispersion of chemical shifts for $\mathbf{H_\delta}$ and $\mathbf{H_\gamma}$ will only make the overall multiplet wider).

The multiplet between 1.73 and 1.66 ppm is attributed to four overlapping methylene proton signals of the $RC(\mathbf{H_\pi})_2CH{=}CHC(\mathbf{H_{\pi'}})_2R'$ group.

As expected, the multiplet for $\mathbf{H_\delta}$ and $\mathbf{H_\gamma}$ correlates with the multiplet for $\mathbf{H_\pi}$ and $\mathbf{H_{\pi'}}$ in both COSY and TOCSY spectra, indicated by the cross peak at {4.99,1.69} in Figs. 11 and 12 respectively. From HSQC and HMBC spectra (Figs. 9 and 10 respectively) it could be found that the corresponding carbon peaks for $\mathbf{C_\Delta}$ and $\mathbf{C_\Gamma}$ are at 128.65 and 128.50 ppm respectively, and peaks for $\mathbf{C_\Pi}$ and $\mathbf{C_{\Pi'}}$ are overlapping and are presented as an apparent singlet at 26.17 ppm.

Based on the ^1H and ^{13}C NMR spectra (Figs. 7 and 8 respectively), the triglyceride molecule adopts the C_s symmetry in melt.

The multiplet for the unique hydrogen atom $\mathbf{H_c}$ appears between 4.90 and 4.83 ppm. The corresponding carbon atom $\mathbf{C_C}$ at 68.09 in the ^{13}C spectrum has been identified from the {4.87,68.09} cross peak in HSQC spectrum (Fig. 9) and clearly belongs to a methine group evidenced by the negative peak in DEPT135 (Fig. 8).

Table 2 Detailed assignment of NMR spectra.

Atom								
^{13}C	^{1}H	^{13}C/C&H-type (from DEPT135)	^{1}H/mult/^{x}J	HSQC[a]	HMBC[a]	COSY[a]	TOCSY[a]	ROESY[a]
A	–	170.64, C=O			(A+A'):d (A+A'):d'			
A'	–	170.35, C=O						
Δ	**δ+γ**	128.65, CH	5.02-4.94, 2H, m (overall width 26 Hz, *cis* CH=CH)	Δ:(δ+γ)	(Δ+Γ):(π+π') (Π+Π'):(δ+γ)	(δ+γ):π	(δ+γ):π	
Γ		128.50, CH		Γ:(δ+γ)				
C	**c**	68.09, CH	4.90-4.83, 1H, m	C:c	C:d C:d'	c:d c:d'	c:d:d'	c:d
D	**d+d'**	60.85, CH_2	d: 3.94, 2H, dd. d': 3.76, 2H, dd. $^{2}J_{d\text{-}d'} = 11.94$ Hz, $^{3}J_{c\text{-}d} = 4.17$ Hz, $^{3}J_{c\text{-}d'} = 6.09$ Hz	D:(d+d')	(D+D):d (D+D):d'	d:d' c:d c:d'	c:d:d'	c:d d:d' d:(f+f') d':(f+f')
E+E'	**e+e'**	32.68, CH_2	1.91, t, 6H, $^{3}J_{e/e'\text{-}g/g'} = 7.23$ Hz	(E+E'):(e+e')		(e+e'):(g+g')	(e+e'):(f+f'):(g+g'):(h+h')	
F+F'	**f+f'**	peaks between 35.14-16.97	0.96, br app s, 54H	(F+F'):(f+f')			(e+e'):(f+f'):(g+g'):(h+h')	d:(f+f') d':(f+f')

Continued

Table 2 Detailed assignment of NMR spectra.—cont'd

Atom								
^{13}C	^{1}H	^{13}C/C&H-type (from DEPT135)	^{1}H/mult/^{x}J	HSQC[a]	HMBC[a]	COSY[a]	TOCSY[a]	ROESY[a]
Π+Π'	**π+π'**	26.17, CH_2	1.73-1.66, m, 4H	(Π+Π'): (π+π')	(Δ+Γ): (π+π') (Π+Π'): (δ+γ)	(δ+γ):π	(δ+γ):π	
G+G'	**g+g'**	23.82, CH_2	1.32-1.20, m, 6H	(G+G'): (g+g')		(e+e'): (g+g')	(e+e'): (f+f'): (g+g'): (h+h')	
H+H'	**h+h'**	12.83, CH_3	h: 0.56, t, 6H, $^{3}J_{f\text{-}h} = 7.06$ Hz h': 0.60, t, 3H, $^{3}J_{f'\text{-}h'} = 7.33$ Hz	(H+H'): (h+h')			(e+e'): (f+f'): (g+g'): (h+h')	

[a] Unreliable cross-peaks are not included.

Proton $\mathbf{H_c}$ independently couples with diastereotopic groups of protons $\mathbf{H_d}$ and $\mathbf{H_{d'}}$. These $\mathbf{H_d}$ and $\mathbf{H_{d'}}$ appear as two doublets of doublets centred at 3.94 and 3.76 ppm respectively, showing the expected ^2J and ^3J coupling constants (see Fig. 7 for spectrum and Table 2 for coupling constant values). Expected correlations between protons $\mathbf{H_c}$, $\mathbf{H_{d\ and\ H_{d'}}}$ are seen in COSY and TOCSY spectra (Figs. 11 and 12 respectively and Table 2). In HSQC spectrum (Fig. 9), both pairs of $\mathbf{H_d}$ and $\mathbf{H_{d'}}$ correlate (cross peaks at {3.95,60.85} and {3.76,60.85} respectively) with the carbon atoms $\mathbf{C_D}$ which resonates at 60.85 ppm in its ^{13}C spectrum (Fig. 8). Expected cross-peaks between $\mathbf{H_c}$, $\mathbf{H_d}$ and $\mathbf{H_{d'}}$, and $\mathbf{C_C}$ and $\mathbf{C_{D,}}$ are observed in the HMBC spectrum (Fig. 10 and Table 2).

As expected for the C_s symmetric compound, the acyl group connected to $\mathbf{C_C}$ is unique; it's proton and carbon environments are designated as **a'**, **e'-h'** and **A'**, **E'-H'** respectively. The two remaining acyls connected to two carbon atoms $\mathbf{C_D}$ are equivalent and their proton and carbon environments are designated as **a**, **e-h** and **A**, **E-H** respectively. The chemical shifts for these two acyl environments are very similar and the only two solid pieces of evidence which allow to distinguish between these are (i) the two partially overlapping triplets for the methyl groups (at 0.56 ppm for $\mathbf{H_h}$ and 0.60 ppm for $\mathbf{H_{h'}}$) in the ^1H NMR (Fig. 7 and Table 2) and the distinguishable carbonyl carbon atom peaks at 170.64 ppm for $\mathbf{C_A}$ and 170.35 ppm for $\mathbf{C_{A'}}$, respectively (Fig. 8 and Table 2). Apparent triplet at 1.91 ppm assigned to $\mathbf{H_{e+e'}}$ and peaks ascribed to $\mathbf{H_{f+f'}}$ (0.96 ppm, broad apparent singlet) and $\mathbf{H_{g+g'}}$ (1.32–1.20 ppm, multiplet) are overlapping and cannot be distinguished between different acyl environments. All individual peaks assigned to acyl environments show expected correlations in COSY and TOCSY spectra (Figs. 11 and 12). Corresponding carbon environments for $\mathbf{C_{E+E'}}$, $\mathbf{C_{F+F'}}$, $\mathbf{C_{G+G'}}$ and $\mathbf{C_{H+H'}}$ were assigned with the help of HSQC and can be found at 32.68, 35.14–16.97, 23.82 and 12.83 respectively.

NMR integration allows to establish the acyl chain length with the reasonable degree of accuracy, and corresponds to $C(=O)(CH_2)_{11}CH_3$ assuming that all three chains are the same.

Intermolecular interactions were examined using ROESY NMR spectroscopy (Fig. 13). This showed the expected cross peaks responsible for the interactions between $\mathbf{H_d}$ and $\mathbf{H_{d'}}$ at {3.95,3.75} and also between $\mathbf{H_c}$ and $\mathbf{H_d}$ at {4.87,3.95}; at the same time the absence of the through-space interactions between $\mathbf{H_c}$ and $\mathbf{H_{d'}}$ further confirms the spacial arrangement of $\mathbf{H_c}$, $\mathbf{H_d}$ and $\mathbf{H_{d'}}$ (*e.g.* $\mathbf{H_c}$ and $\mathbf{H_d}$ being on one side of the molecule and $\mathbf{H_c}$ and $\mathbf{H_{d'}}$ on opposite sides). The only other clearly observable cross peaks at {3.95,0.96} and {3.75,0.96} are responsible for the interactions between the bulk of CH_2 groups and protons $\mathbf{H_d}$ and $\mathbf{H_{d'}}$. This could be explained either by (i) the "folding" of at least one acyl chain around the glycerol backbone (=intramolecular interactions), or by (ii) the existence of intermolecular interactions between two triglyceride molecules or by (iii) the existence of intermolecular interactions between one triglyceride molecule and the unsymmetrical alkene $RCH_2CH{=}CHCH_2R'$ molecules.

6. Physical properties of butter oil

Butter oil appears semi-solid at room temperature with pale yellow color and grainy texture. It is not soluble in or miscible with water, but it is soluble in some organic solvents namely acetone, hexane, chloroform, benzene, isopropanol and diethyl ether. Butter and brown residue, on the other hand, are not fully soluble in these or even in more polar solvents. Solubility of butter, butter oil and brown residue was determined in various polar and non-polar solvents; the results are tabulated in Table 3.

Butter oil is composed of lipids; hence the non-polar solvents are highly suitable for its dissolution, however, butter contains carbohydrates and proteins which are not readily soluble in aqueous or non-polar environments alone. Brown residue is a result of non-enzymatic browning known to be a Maillard reaction involving cascade of complex reactions [19,28], components of which are insoluble (Table 3) in common solvents. The sticky mass in brown residue is butter oil, which dissolves in hexane and leaves out free-flowing brown powder (Fig. 1).

Density of butter oil obtained from three different sources were measured using Density meter DMA 4200 M (Anton Paar Ltd, St Albans, UK). Density of a butter oil is lower than water, and it decreases with increasing temperature (Fig. 14). The values are tabulated in Table 4. Densities of all butter oils studied in this work are comparable at 20 °C and 40 °C (molten state), however they differ at 25 °C perhaps due to difference in compositions of mixed triglycerides.

Table 3 Solubility of butter oil, butter and brown residue in various solvents at ambient conditions.

No	Solvents	Butter oil	Butter	Brown residue
1.	Dimethyl sulfoxide (DMSO)	Not soluble	Not soluble	Slightly soluble
2.	Dimethylformamide (DMF)	Not soluble	Not soluble	Slightly soluble
3.	Glycerol	Not soluble	Not soluble	Less soluble than above
4.	Glycerol + DMF	Not soluble	Not soluble	Slightly soluble
5.	Glycerol + DMSO	Not soluble	Not soluble	Slightly soluble
6.	Glycerol + Methanol	Not soluble	Not soluble	Slightly soluble
7.	Methanol	Not soluble	Not soluble	Less soluble
8.	Ethanol	Not soluble	Not soluble	Less soluble
9.	Acetone	Soluble (1 g/1 mL)	Slightly soluble	Not soluble
10.	Hexane	Soluble (1 g/1 mL)	Slightly soluble	Not soluble
11.	Acetonitrile	Not soluble	Not soluble	Not soluble
12.	Chloroform	Soluble (1 g/1 mL)	Slightly soluble	Slightly soluble
13.	Hot water	Not soluble	Not soluble	Slightly soluble
14.	Benzene	Soluble (1 g/1 mL)	Slightly soluble	Less soluble
15.	Isopropyl alcohol	Soluble (1 g/1 mL)	Slightly soluble	Less soluble
16.	Diethyl ether	Soluble (1 g/1 mL)	Slightly soluble	Less soluble

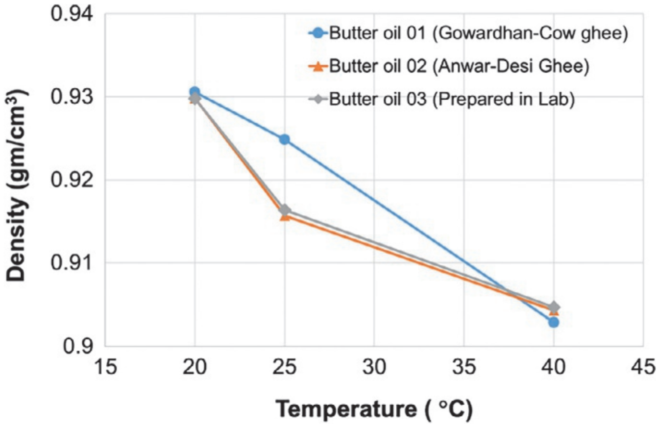

Fig. 14 Density values of butter oils obtained from different sources. A decrease in density with temperature is evident from the corresponding curves.

Table 4 Density of various butter oils (values in gm/cm^3).

Temperature (°C)	**20**	**25**	**40**
Butter oil 01 (Gowardhan-Cow Ghee)	0.93057	0.92487	0.90283
Butter oil 02 (Anwar-Desi Ghee)	0.92984	0.91568	0.90427
Butter oil 03 (Prepared in Lab)	0.92981	0.91637	0.90464

7. Thermal behavior of butter oil

Mettler Toledo differential scanning calorimetry (DSC) (DSC 823, Switzerland) and thermo-gravimetric analysis (TGA) (TGA/SDTA 851^e, Switzerland) were used for thermal characterization of butter and butter oil. About 10 mg of sample was carefully added to 40 μL Aluminum pans. TGA was performed on samples to get decomposition profile, followed by DSC. About 7–8 mg sample was carefully added to a DSC pan that was then hermetically sealed using Mettlor press; an empty hermetically sealed aluminum pan was used as a reference. TGA experiments were carried out from 25 to 500 °C using a heating rate of 2 °C/min whereas isothermal heating, cooling and heating DSC scans were performed from −50 to 120 °C at the rate of 2 °C/min. STAR^e software, Version 9.0X, was used to analyze the thermogravimetric data.

Butter oil hardly contains any water, so ice melting (around 0 °C) and water vaporization (>100 °C) transitions observed for butter are not present in its differential scanning calorimetry (DSC) scan (Fig. 15A). Butter also

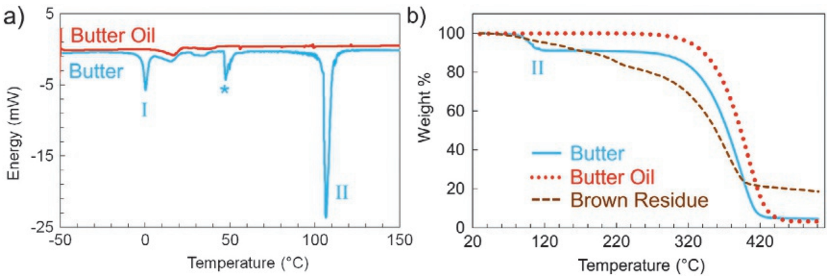

Fig. 15 (A) Differential scanning calorimetry (DSC) profiles for butter and butter oil and (B) thermogravimetric analysis (TGA) of butter, butter oil and brown residue. "I" and "II" illustrate unique transitions in butter oil due to presence of water whereas "*" indicates transition possibly due to presence of non-lipid components [19] (protein rearrangement upon lipid melting).

shows transition around 50 °C which could be due to structural rearrangement of non-lipid components when lipids around them are melted. Broad melting transitions around 15 °C and 35 °C seen in both butter and butter oil; this could be due to phase transitions among lipid polymorphs.

Butter oil is generally used for high temperature cooking [1], the reason of which is obvious from the thermogravimetric analysis graph (Fig. 15B); it does not decompose until 300 °C. Butter has a transition around 100 °C owing to the presence of water whereas other components start to decompose at lower temperature than that of butter oil. Brown residue shows several transitions and even at about 500 °C it does not decompose completely.

8. Conclusions

Butter oil and its precursor butter display lamellar phases, as detected by SAXS analysis (Figs. 2–4). Further polymorphism, detected by WAXS, shows presence of fluid lamellar (L_α) and crystalline lamellar (L_C) nanostructures (Figs. 2–4). β and β' polymorphs commonly seen for food fats were also identified with their characteristic WAXS signals. Raising the temperature to 37 °C caused partial melting of lamellar phase in butter whereas it was completely molten in case of the butter oil (Fig. 3). The effect of hydration was not too significant as the butter oil is not miscible with water. Therefore, to improve its applicability to suit aqueous systems, it needs to be modified; this can be achieved either by its emulsification using surfactant stabilizers [11] or mixing with other amphiphilic molecules [12] that can enhance its water solubility.

Butter shows densely packed microstructures composed of carbohydrates, proteins and lipids. This further encapsulates water and/or fatty droplets whereas butter oil does not contain carbohydrates and proteins, hence shows a different texture without discrete droplets (Fig. 5). Thermal transitions typical of water containing samples were observed for butter studied by DSC while butter oil did not show transitions around 0 °C and 100 °C. Also, a transition around 50 °C (could be protein denaturation in butter) was not seen for butter oil. Butter oil displays good thermal stability as compared to butter and brown residue (Fig. 15) as investigated by TGA.

The presence of carbohydrates and proteins (in butter oil and brown residue) with corresponding functional groups of —OH and —NH was concluded based on FTIR analysis (Fig. 6), whereas butter oil does not show signals in this region of IR spectrum. NMR spectra confirms the abundance of triglycerides in butter oil studied in pure form (without any solvent) melted at 50 °C, the molecular structure of triglyceride was elucidated from multinuclear NMR data and ROESY spectroscopy confirmed that glycerol backbone protons are involved in through-space interactions with CH_2 protons (Figs. 7-13). Butter oil is soluble in non-polar solvents as it primarily contains lipids, but butter and brown residue, containing non-lipid components were not fully soluble in any non-polar or even polar solvents. This work shades light on the nanostructural properties of butter oil, particularly SAXS/WAXS characterization at various temperatures. It is potentially useful for developing butter oil formulations for various active molecules [12].

Acknowledgments

We would like to thank a visiting student Mr Younes Turki (Pierre and Marie Curie University, Paris, France) and a project student Ms Amelia Smith (UCLan) for preliminary work and Mr James Donnelly and Mr Patric Cookson for technical support. We acknowledge Mr Nick Spencer (University of Reading) for support on X-ray scattering work.

References

[1] B.M. Mehta, in: R.A. Moreau, A. Kamal-Eldin (Eds.), 21—Butter, Butter Oil, and Ghee, in Gourmet and Health-Promoting Specialty Oils, AOCS Press, 2009, pp. 527–559.

[2] M.L. Sserunjogiab, R.K. Abrahamsena, J. Narvhusa, A review paper: current knowledge of ghee and related products, Int. Dairy J. 8 (1998) 677–688.

[3] M.V. Kumar, K. Sambaiah, B.R. Lokesh, Effect of dietary ghee—the anhydrous milk fat, on blood and liver lipids in rats, J. Nutr. Biochem. 10 (2) (1999) 96–104.

[4] M.J. McCarthy, A. Kuksis, J.M.R. Beveridge, Composition of molecular distillates of butter oil: isolation and identification of components other than glycerides, J. Lipid Res. 5 (1964) 609–615.

[5] M. Harold, On Food and Cooking: The Science and Lore of the Kitchen, Scribner, New York, 2004.

[6] J.K. Amamcharla, R. Singh, Butter oil and ghee, in: P.L.H. McSweeney, J.P. McNamara (Eds.), Encyclopedia of Dairy Sciences, third ed., Academic Press, Oxford, 2022, pp. 695–706.

[7] A. Kumar, et al., Ghee: its properties, importance and health benefits, Lipid Univ. 6 (2018) 6–14.

[8] A. Mahakalkar, P. Kashyap, R.B.B. Hatwar, The versatility of cow ghee—an ayurvedaperspective, J. Drug Deliv. Ther. 1 (2014) 28–34.

[9] E.M. Shah, Base Material for Pharmaceutical and/or Cosmetic Cream (Herbal Composition for Itchy or Infected Skin), Google Patents, 2014.

[10] P. Deshpande, K. Kulkarni, Production and evaluation of biodiesel from palm oil and ghee (clarified butter), Chem. Proc. Eng. Res. 2 (2012) 33–42.

[11] C.V. Kulkarni, Ultrasonic processing of butter oil (ghee) into oil-in-water emulsions, J. Food Process. Preserv. 41 (2017) e13170.

[12] A.A. Sunny, et al., Butter oil and derived lipid-formulations for delivery of poorly soluble small drug molecules, in: 6th Edwards Symposium—Soft Matter for the 21st Century, Cambridge, UK, 2022.

[13] A. Alkhalifah, H. Alkahtani, Composition of ghee (Samn-Barris) from cows and sheeps milk, Food Chem. 46 (4) (1993) 373–375.

[14] W. Ben Amara-Dali, et al., Anhydrous goat's milk fat: thermal and structural behavior. 1. Crystalline forms obtained by slow cooling, J. Agric. Food Chem. 53 (26) (2005) 10018–10025.

[15] S. Danthine, Physicochemical and structural properties of compound dairy fat blends, Food Res. Int. 48 (1) (2012) 187–195.

[16] A.E. Fatouh, et al., Chemical and thermal characteristics of buffalo butter oil fractions obtained by multi-step dry fractionation, Lebensmittel-Wissenschaft Und-Technologie 36 (5) (2003) 483–496.

[17] C. Lopez, et al., Milk fat and primary fractions obtained by dry fractionation—1. Chemical composition and crystallisation properties, Chem. Phys. Lipids 144 (1) (2006) 17–33.

[18] A. Newton, Flavour formation in ghee, in: Biology, University of Canterbury, New Zealand, 2014, p. 193.

[19] J.A. Rufián-Henares, S. Pastoriza, Maillard reaction, in: B. Caballero, P.M. Finglas, F. Toldrá (Eds.), Encyclopedia of Food and Health, Academic Press, Oxford, 2016, pp. 593–600.

[20] USDA, United States Department of Agriculture (USDA) National Nutrient Database for Standard Reference Release 28, 2016.

[21] S.M. van Ruth, et al., Butter and butter oil classification by PTR-MS, Eur. Food Res. Technol. 227 (1) (2008) 307–317.

[22] N. Kumar, et al., Chapter 10—Flavor addition in dairy products: health benefits and risks, in: R.R. Watson, R.J. Collier, V.R. Preedy (Eds.), Nutrients in Dairy and their Implications on Health and Disease, Academic Press, 2017, pp. 123–135.

[23] S. Martini, A.G. Marangoni, Microstructure of dairy fat products, in: Structure of Dairy Products, Blackwell Publishing Ltd., 2007, pp. 72–103.

[24] A. Sadeghpour, et al., Global small-angle X-ray scattering data analysis of triacylglycerols in the molten state (Part I), J. Phys. Chem. B. 122 (45) (2018) 10320–10329.

[25] A.G. Marangoni, S.S. Narine, Physical Properties of Lipids, CRC Press, 2002.

[26] J. Coates, Interpretation of infrared spectra, a practical approach, in: Encyclopedia of Analytical Chemistry, 2000.

[27] R.J. Abraham, J. Fisher, P. Loftus, Introduction to NMR Spectroscopy, Wiley, 1988.

[28] A.E. Newton, et al., The influence of emulsion structure on the Maillard reaction of ghee, Food Chem. 173 (2015) 1243–1249.

This page intentionally left blank

CHAPTER TWO

Fermi gas mediates an attractive force between two parallel planes of equal charge

Mitja Drab[a,*] **and Veronika Kralj-Iglič**[b,c]
[a]Laboratory of Physics, Faculty of Electrical Engineering, University of Ljubljana, Ljubljana, Slovenia
[b]Laboratory of Clinical Biophysics, Chair of Orthopaedic Surgery, Faculty of Medicine, University of Ljubljana, Ljubljana, Slovenia
[c]Laboratory of Clinical Biophysics, Faculty of Health Sciences, University of Ljubljana, Ljubljana, Slovenia
*Corresponding author: e-mail address: mitja.drab@fe.uni-lj.si

Contents

Abstract

The main mechanism of energy storage at the nanoscale remains the electric double layer (EDL) composed of a charged surface and a diffuse layer of opposite charge with quantum treatment often being neglected. We recently showed that charged Fermi gas between two oppositely charged and equal plane-parallel planes results in a repulsive force between them. Here, we present a new branch of solutions to the same variational problem resulting in overall higher energy densities and find cases where the force between two like-charged surfaces is attractive and of the order of piconewtons per square nanometer. We find that the corresponding solutions' differential capacitance is on the order of classic Poisson-Boltzmann theory of the EDL. These results may be significant in biological systems where adhesion and interaction between charged surfaces is ubiquitous.

Advances in Biomembranes and Lipid Self-Assembly, Volume 36
ISSN 2451-9634
https://doi.org/10.1016/bs.abl.2022.10.002

1. Introduction

Physical and chemical properties of a material at the nanoscale can be highly different from the same material at the bulk scale, since most of the constituent atoms in the former case are located at or near the surface. Nanomaterials are defined with one of the dimensions being between 1 and 100 nm. At these scales, quantum effects may be important. Recent years have seen a rapid development of material manipulation at the nanoscale [1–4] ranging from biocompatible materials for use in medicine [5–7] and nanoscale biosensors to nanocapacitors [8,9]. In biology, quantum effects may be important at the interfaces of tissues and biomolecules. For example, there is evidence that DNA mutations are prominently driven by tunneling of protons between bases [10] while photosynthesis and magnetoreception is driven by effects of the sub-atomic scales.

The main mechanism of passive energy storage devices in biology is the electric double layer (EDL), a phenomenon that occurs on the interface of an electrolyte in contact with a charged surface [11]. Since ions in the electrolyte carry an electric charge, the charged surface attracts ions of the opposite charge (counterions) and repels ions of the same charge (coions). A competing force that mediates ion concentrations is diffusion; far away from the charged surface where electric fields go to zero the concentrations of both types of ions are taken to be the same. Thermodynamic equilibrium is attained when electrostatic effects are in balance with the effects of diffusion. This results in the accumulation of counterions and depletion of like-charged coions near the charged surface.

The first mathematical description of the EDL of a monovalent electrolyte was given a century ago by the work of Gouy and Chapman, whose major contribution was the Poisson-Boltzmann equation that rigorously expressed the competition between electrostatic and mixing effects [12,13]. Within the Gouy-Chapman model the ions were monovalent, point-like and devoid of direct interactions. They were imbedded in a continuum of a constant dielectric permittivity. The ions and surfaces contributed to a mean electric field within the system, implying a mean-field approximation. Since then, the EDL theory has been upgraded in many ways [14]. One of the first things taken into account were steric effects that included finite ion sizes, while later models included the dipole nature of water of the electrolyte solution [15–18]. Bikerman advanced the theory of Gouy by considering the hydration shells of water around charged ions and concluded that dipole moments of ions, and their hydration shells, are decisive in the competition of ions and solvent molecules for positions near the charged surface [19]. Further investigations considered orientational ordering of water molecules near the charged surface, resulting in a coordinate-dependent dielectric permittivity of the electrolyte [20,21].

A relevant quantity of EDL-based systems is their Helmholtz free energy, a thermodynamic potential that attains its minimum value in cases when volume and temperature are held constant [22]. In the Poisson-Boltzmann theory of EDL, where particles contained between two like-charged surfaces are taken to be monovalent, point-like and noninteracting, the dependency of Helmholtz free energy is a monotonically decreasing function of surface separation. This implies a repelling force between the charged surfaces. However, it is experimentally known that like-charged surfaces can be attracted to, and oppositely charged surfaces can be repelled from, each other in the presence of multivalent counterions [23–25]. In biology, condensation of DNA, which corresponds to the packing of DNA in viruses, network formation in actin solutions, and aggregation of rodlike M13 viruses, are some of the examples where electrostatic interactions mediated by multivalent ions are important. This has inspired many efforts to understand the interaction between objects with different shapes and charge distributions [26]. Models that include finite sizes of ions or ions with multivalent or quadrupolar charge distributions can lead to a minimum of the Helmholtz free energy, defining regions of the phase-space where attraction between two like-charged surfaces is possible. The main mechanism of such attraction are ion-ion correlations and bridging effects due to orientational ordering of ions [27,28].

Little attention has been given to a quantum treatment of the electric double layer, with some exceptions that focused on the wave functions of electrons at the electrode interface [29]. A quick survey of the field confirms that most research is centered on the engineering aspects of electrodes and electrolytes to yield higher energy and power densities, yet quantum effects are likely to be important at the scales of capacitors manufactured at the nanoscale. In the present paper, we consider a model of a nanocapacitor with quantum particles with half-integer spin—fermions. Our previous work has shown that consideration of symmetry of wavefunctions of fermions and quantum statistics can give rise to diffuse layers of fermions between two equally charged surfaces [30,31]. However, our results were limited only to one of two possible branches of solutions. In the derived differential equation for mean electric potential of the system we only focused on the positive square root of the electric field derivative, leaving out the second half of the solution. In the present paper, the equation is solved for the previously disregarded root, leading to different approximate analytical solutions of potential and particle number densities. The distinction of both branches of solutions becomes most apparent when Helmholtz free energy is calculated as function of surfaces separation. We find a minimum of the Helmholtz free energy at certain system parameters, implying an attractive force between the surfaces.

2. Theoretical background

The model system consists of a single type of negatively charged fermions confined between two large planar yz surfaces at $x=0$ and at $x=d$. Each surface carries a uniformly distributed positive charge with surface charge density $\sigma \geq 0$. A generalization to positively charged particles and negatively charged surfaces is straightforward and analogous. The entire system is electrically neutral. The fermions are subject to the constraints on available eigenenergy states implied in the Fermi-Dirac statistics while the effect of the electric field on the wavefunctions and on the energy states is not considered. These states can be either occupied or unoccupied, with the probability that energy level ε_{n} is occupied being

$$f_{\mathrm{n}} = \frac{1}{1 + \exp\left((\varepsilon_{\mathrm{n}} - \mu)/k_B T\right)}, \tag{1}$$

where μ is the Lagrange coefficient for the constraint requiring fixed total number of particles in the system, k_B is the Boltzmann constant and T is absolute temperature [22]. For simplicity we take that each particle is confined to an infinite three dimensional square potential well so that its energy is given by quantized discrete values

$$\varepsilon_{\mathrm{n}} = \frac{\mathrm{n}^2 h^2}{8ml^2}, \quad \mathrm{n} = 1,2,3,\ldots \tag{2}$$

Here, h is the Planck constant, m is the particle mass and l is the extension of the potential well. Following the derivation from our previous work (see [30]), we derive the Lagrange function for dimensionless particle density $n(x)$ and mean electric field $E(x)$ in the system:

$$\mathcal{L} = \alpha n^{\frac{5}{3}}(x) + E^2(x) - \lambda(x)\left(\frac{\partial E(x)}{\partial x} + 2n(x)\right) + \tilde{\lambda} n(x), \tag{3}$$

where $\lambda(x)$ and $\tilde{\lambda}$ are the local and global Lagrangian multipliers ensuring the validity of Gauss law and a constant number of particles between the plates, respectively. The dimensionless constant α is equal to

$$\alpha = \frac{3}{5\sqrt[3]{2}}\left(\frac{3}{\pi}\right)^{2/3}\frac{h^2\varepsilon_0}{me_0^{5/3}}\frac{1}{\sqrt[3]{\sigma d^5}}. \tag{4}$$

Here, e_0 is elementary charge carried by each particle and ε_0 the permittivity of vacuum. Separation between the charged surfaces is given by d. Minimization of the Lagrange function is performed with respect to dimensionless unknown functions $n(x)$ and $E(x)$. The nondimensional quantities were normalized

$$x = \tilde{x}/d, \quad n = \tilde{n}/n_0, \quad E = \tilde{E}/E_0, \tag{5}$$

where tilde marks position $\tilde{x}$, number particle density $\tilde{n}$ and electric field $\tilde{E}$ with dimensions. The normalization constants are related to values for a classic parallel plate capacitor:

$$n_0 = \frac{2\sigma}{de_0}, \quad \phi_0 = \frac{\sigma d}{\varepsilon_0} \quad \text{and} \quad E_0 = \frac{\sigma}{\varepsilon_0}. \tag{6}$$

Here, ϕ_0 marks electric potential. Considering the relation $E(x) = -\,\mathrm{d}\phi/\mathrm{d}x$, the Euler-Lagrange equations give the equation for ϕ:

$$\left(\frac{\mathrm{d}^2\phi(x)}{\mathrm{d}x^2}\right)^{2/3} = \left(\frac{\beta\sqrt{5}}{4}\right)^2\left(4\phi(x) - \tilde{\lambda}\right). \tag{7}$$

Here, β is the nondimensional constant

$$\beta = 4\sqrt{\frac{2}{5}}\left(\frac{3}{5\alpha}\right)^{3/4}. \tag{8}$$

The symmetry of the system imposes the electric field to be zero between the surfaces

$$\frac{\mathrm{d}\phi}{\mathrm{d}x}\Big|_{x=1/2} = 0, \tag{9}$$

with electric potential there being constant. We may set the constant value there to zero without loss of generality.

$$\phi\left(x = \frac{1}{2}\right) = 0. \tag{10}$$

The other boundary condition follows from electroneutrality of the system

$$\frac{\mathrm{d}\phi}{\mathrm{d}x}\Big|_{x=0} = -1. \tag{11}$$

In summary, all previously discussed conditions still apply (for details in derivation, see [30]).

3. Derivation of analytic solutions

After taking the square root of Eq. (7), both positive and negative roots must be considered. Since the real-valued root of Eq. (7) was investigated in our previous work [30], we consider the other branch of solutions. It is not obvious that $\tilde{\lambda}$ should be a positive quantity, so we are interested in the case where the right side of Eq. (7) is negative,

$$4\phi < \tilde{\lambda}. \tag{12}$$

Eq. (7) is now

$$\frac{\mathrm{d}^2\phi}{\mathrm{d}x^2} = (-1)^{3/2}\left(\frac{\beta\sqrt{5}}{4}\right)^3 (\tilde{\lambda} - 4\phi)^{3/2}. \tag{13}$$

Since $(-1)^{3/2} = i$, where i is the imaginary unit, we obtain

$$\frac{\mathrm{d}^2\phi}{\mathrm{d}x^2} = (-i)\left(\frac{\beta\sqrt{5}}{4}\right)^3 (\tilde{\lambda} - 4\phi)^{3/2}. \tag{14}$$

We introduce a new variable

$$u = \tilde{\lambda} - 4\phi, \qquad \mathrm{d}u = -4\mathrm{d}\phi, \tag{15}$$

and make use of the identity

$$\frac{\mathrm{d}}{\mathrm{d}x}\left(\frac{\mathrm{d}\phi}{\mathrm{d}x}\right)^2 = 2\frac{\mathrm{d}^2\phi}{\mathrm{d}x^2}\frac{\mathrm{d}\phi}{\mathrm{d}x}. \tag{16}$$

For compactness, we label the constant $a = \beta\sqrt{5}/4$. If we multiply both sides of Eq. (14) with $2\ \mathrm{d}\phi/\mathrm{d}x$, we obtain

$$2\frac{\mathrm{d}\phi}{\mathrm{d}x}(-i)a^3u^{3/2} = 2\frac{\mathrm{d}^2\phi}{\mathrm{d}x^2}\frac{\mathrm{d}\phi}{\mathrm{d}x}. \tag{17}$$

Using the chain rule

$$\frac{\mathrm{d}u}{\mathrm{d}x} = \frac{\mathrm{d}u}{\mathrm{d}\phi}\frac{\mathrm{d}\phi}{\mathrm{d}x}, \tag{18}$$

Eq. (17) can be restructured

$$2\left(\frac{\mathrm{d}u}{\mathrm{d}x}\cdot\frac{\mathrm{d}\phi}{\mathrm{d}u}\right)(-i)a^3u^{3/2} = \frac{\mathrm{d}}{\mathrm{d}x}\left(\frac{\mathrm{d}u}{\mathrm{d}x}\cdot\frac{\mathrm{d}\phi}{\mathrm{d}u}\right)^2. \tag{19}$$

Since $\mathrm{d}\phi/\mathrm{d}u = -1/4$, it follows that

$$\frac{i}{2}a^3u^{3/2}\mathrm{d}u = \frac{1}{16}\mathrm{d}\left(\frac{\mathrm{d}u}{\mathrm{d}x}\right)^2. \tag{20}$$

Integrating both sides of the equation yields

$$\frac{16}{5}a^3i\left(u^{5/2} - u_{1/2}^{5/2}\right) = \left(\frac{\mathrm{d}u}{\mathrm{d}x}\right)^2. \tag{21}$$

Here, the boundaries of integration run from $x \in [0, 1/2]$. By symmetry of the system, we assume that the reduced electric field is zero at the midline,

$$\frac{\mathrm{d}u}{\mathrm{d}x}\Big|_{x=1/2} = 0. \tag{22}$$

Since we are interested in finding an analytical solution, we use the approximation in changing the power from $5/2 \rightarrow 2$. Circumventing this step results in functions that are not integrable analytically, but qualitatively similar as described in [30]. Therefore,

$$\frac{\mathrm{d}u}{\mathrm{d}x} = \sqrt{\frac{16}{5}a^3i}\left(u^2 - u_{1/2}^2\right)^{1/2}. \tag{23}$$

The square root of the imaginary unit $\sqrt{i} = \left(\sqrt{2}/2\right)(1 + i)$. Separating the variables and integrating on both sides within the boundaries $x \in [1/2, x]$ gives

$$\frac{u + \sqrt{u^2 - u_{1/2}^2}}{u_{1/2}} = \exp\, c\left(\frac{1}{2} - x\right), \tag{24}$$

where $c = 2(1 + i)\sqrt{2a^3/5}$. After some rearranging we arrive at the expression for the reduced potential u:

$$u = u_{1/2}\cosh\, c\left(x - \frac{1}{2}\right). \tag{25}$$

Considering the identity for complex arguments of hyperbolic functions

$$\cosh(a+bi) = \cosh a \cos b + i \sinh a \sin b, \tag{26}$$

we may separate the reduced potential dependency into a sum of real and complex terms, namely

$$u = u_{1/2}\left(\cosh k\left(x-\frac{1}{2}\right)\cos k\left(x-\frac{1}{2}\right) + i\sinh k\left(x-\frac{1}{2}\right)\sin k\left(x-\frac{1}{2}\right)\right), \tag{27}$$

where the constant k is now real-valued and equal to

$$k = 2\sqrt{\frac{2a^3}{5}}. \tag{28}$$

We examine the boundary conditions of our system to determine the constant $u_{1/2}$. The electrically charged surface at $x=0$ imposes that the normalized electric field there is equal to -1:

$$\frac{\mathrm{d}\phi}{\mathrm{d}x}\Big|_{x=0} = -1. \tag{29}$$

Considering the substitution, we equate the real part of potential since only real-valued potential is physically relevant:

$$\mathrm{R}\left(\frac{\mathrm{d}u}{\mathrm{d}x}\right)\Big|_{x=0} = -4\frac{\mathrm{d}\phi}{\mathrm{d}x}\Big|_{x=0} = (-4)\cdot(-1) = 4. \tag{30}$$

Here, $\mathrm{R}(z)$ denotes the real part of imaginary number z. The derivative $\mathrm{d}u/\mathrm{d}x$ is equal to

$$\frac{\mathrm{d}u}{\mathrm{d}x} = (1+i)ku_{1/2}\sinh\left(k(1+i)\left(x-\frac{1}{2}\right)\right), \tag{31}$$

its real part being

$$R\left(\frac{\mathrm{d}u}{\mathrm{d}x}\right) = ku_{1/2}\left(\cos k\left(x-\frac{1}{2}\right)\sinh k\left(x-\frac{1}{2}\right) - \cosh k\left(x-\frac{1}{2}\right)\sin k\left(x-\frac{1}{2}\right)\right). \tag{32}$$

Satisfying the condition posed in Eq. (30) yields the constant $u_{1/2}$:

$$u_{1/2} = \frac{4}{k\left(\cosh\frac{k}{2}\sin\frac{k}{2} - \cos\frac{k}{2}\sinh\frac{k}{2}\right)}. \tag{33}$$

This constant has a numerical value at given distance between charged surfaces d and their magnitude of surface charge σ. It is worth remembering how the multitude of introduced constants are coupled:

$$k = 2\sqrt{\frac{2a^3}{5}}, \tag{34}$$

$$a = \frac{\beta\sqrt{5}}{4}, \tag{35}$$

$$\beta = 4\sqrt{\frac{2}{5}}\left(\frac{3}{5\alpha}\right)^{3/4}, \tag{36}$$

$$\alpha = \frac{3}{5\sqrt[3]{2}}\left(\frac{3}{\pi}\right)^{2/3}\frac{h^2\varepsilon_0}{me_0^{5/3}}\frac{1}{\sqrt[3]{\sigma d^5}}. \tag{37}$$

The real part of the normalized potential is thus

$$R(u(x)) = \frac{4\cos\left(k\left(x-\frac{1}{2}\right)\right)\cosh\left(k\left(x-\frac{1}{2}\right)\right)}{k\left(\cosh\frac{k}{2}\sin\frac{k}{2} - \cos\frac{k}{2}\sinh\frac{k}{2}\right)}. \tag{38}$$

4. Results and discussion

4.1 Electric potential and particle density

Remembering the substitution given in Eq. (15) we determine the constant $\tilde{\lambda}$ from an arbitrary point, conveniently chosen to be zero between both charged surfaces as noted in Eq. (10). We solve the equation for $\tilde{\lambda}$

$$\begin{aligned} \phi\left(x=\frac{1}{2}\right) &= \frac{\tilde{\lambda} - \mathrm{R}\left(u\left(x=\frac{1}{2}\right)\right)}{4} = 0 \\ \rightarrow \qquad \tilde{\lambda} &= \frac{4}{k\left(\cosh\frac{k}{2}\sin\frac{k}{2} - \cos\frac{k}{2}\sinh\frac{k}{2}\right)}, \end{aligned} \tag{39}$$

and arrive at the result for electric potential between the surfaces:

$$\phi(x) = \frac{1 - \cos\left(k\left(x-\frac{1}{2}\right)\right)\cosh\left(k\left(x-\frac{1}{2}\right)\right)}{k\left(\cosh\frac{k}{2}\sin\frac{k}{2} - \cos\frac{k}{2}\sinh\frac{k}{2}\right)}. \tag{40}$$

The volume density of particles is derived from Euler-Lagrange equations (see [30]):

$$n(x) = \frac{1}{2}\frac{\mathrm{d}^2\phi}{\mathrm{d}x^2}. \tag{41}$$

The real part of this function is

$$n(x) = \frac{k \sin k\left(x - \frac{1}{2}\right) \sinh k\left(x - \frac{1}{2}\right)}{\cosh \frac{k}{2} \sin \frac{k}{2} - \cos \frac{k}{2} \sinh \frac{k}{2}}. \tag{42}$$

Since we require the solutions to be physically relevant, we must always note that the particle density is non-negative,

$$n(x) \geq 0. \tag{43}$$

Before turning our attention to analysis of different values of parameters, let us examine the values of k for which such solutions yield non-negative results. Normalization of the coordinate x in Eq. (5) by the distance between surfaces d assures that the left surface position is at $x=0$ and the right surface at $x=1$, thus constraining the $n(x)$ function domain to be $x \in [0,1]$. The hyperbolic sine in Eq. (42) has a trivial solution at $n(x=1/2)=0$ for any value of k, but non-trivial zeroes require the sine to be zero, imposing the condition

$$\sin k\left(x - \frac{1}{2}\right) = 0 \quad \rightarrow \quad k = \pm 2q\pi, \quad q \in Z. \tag{44}$$

Considering only the first branch of the solutions ($q=1$, $k \in [0, 2\pi]$), we find that the continuous changing of the value k from 0 to 2π is changing the particle density function $n(x)$ as seen in Fig. 1. In the limit $k \to 0$, Eq. (42) becomes $n(x) = 3(1-2x)^2$. For each value of k, $\int_0^1 \mathrm{n(x)dx} = 1$ as demanded by the condition of a constant number of particles.

After surpassing the limit $k=2\pi$, the function value $n(x)$ continually becomes less than zero at $x=0$ and $x=1$, rendering it physically irrelevant. Bearing in mind this limitation, and the fact that the constant k is dependent on the physical parameters of the model (see Eqs. 34–37), we aim to find the extreme limiting parameters of our model. For the parameter $k=2\pi$, the parameter α_{max} is

$$\alpha_{max} = \frac{6}{5}\left(\frac{2}{5^4 \cdot \pi^8}\right)^{1/9}. \tag{45}$$

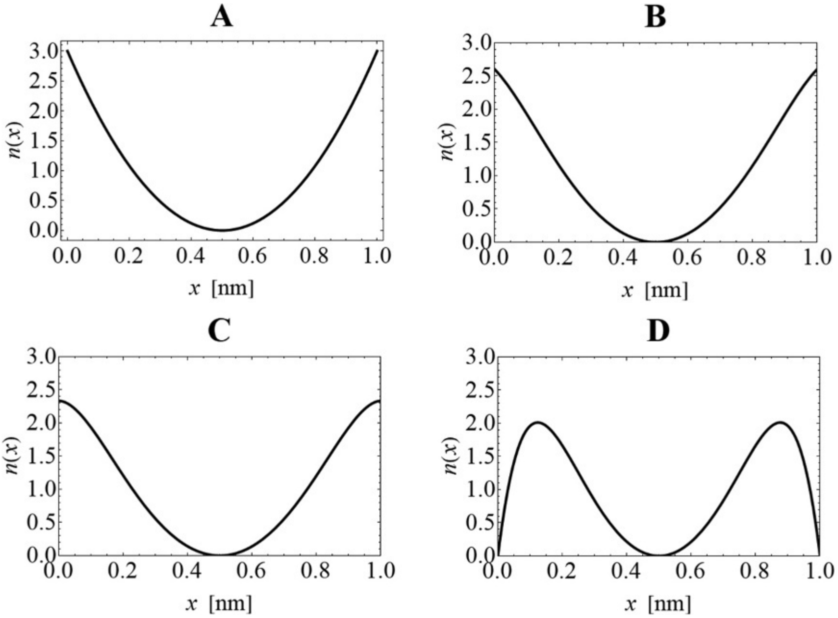

Fig. 1 Particle density (Eq. 42) for different values of k. (A): $k=0$; (B): $k=4\pi/3$; (C): $k=3\pi/2$; (D): $k=2\pi$.

Since α depends on four physical qualities that do not change their value, we may introduce a dimensionless constant K,

$$K = \frac{h^2 \varepsilon_0}{m e_0^{5/3}} \approx 9.05 \cdot 10^{-17}. \tag{46}$$

The main adjustable parameters of our system are the distance between the charged surfaces d and the surface charge density σ. From Eq. (37) we get the relation

$$\sigma_{\max} d^5 = K^3 \left(\frac{3^6 \cdot 5^4 \cdot \pi^2}{2^{13}} \right)^{1/3}. \tag{47}$$

Changing the distance between the charged surfaces d we can find the maximum possible value of $\sigma_{\max}$ where the particle number density is still non-zero over the whole interval. This dependence $\sigma_{\max}(d)$ is seen in Fig. 2.

At fixed distance between the surfaces, the surface charge can only go up to a limited value, as seen in Fig. 2. It is important to note that at fixed distance between the surfaces and below the maximal value $\sigma < \sigma_{\max}$, the results of electric potential, electric field and particle density very much

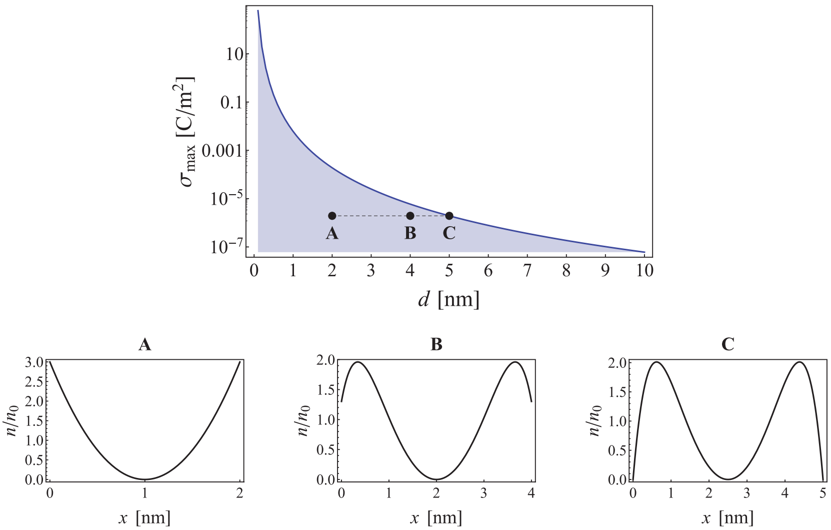

Fig. 2 Dependence of maximum value of $\sigma_{\max}$ at chosen distance between charged surfaces d (Eq. 47) and particle density distributions (Eq. 42) as functions of surfaces separation (A, B, C). Physically relevant solutions with non-zero values of particle number density are found in the shaded part of the graph. The charge density along the line A-B-C is constant and equal to $\sigma_{\max}(d = 5\,\text{nm}) = 1.9\,\mu\text{C/m}^2$.

resemble the case for real-value solutions and PB theory (Fig. 2A), the main difference being the depletion of particles at the midpoint between the surfaces $n(x = d/2) = 0$, while we observe a much more homogenous distribution of particles in the real-value solutions regime [30].

Since we are interested in extreme results, all calculations using $\sigma_{\max}$ were performed with values of surface separation below and at most $d_{\max}$ (see Eq. 47). The further that we take the surfaces apart and toward its maximal allowed value at a given $\sigma_{\max}$, the more the particle density distribution changes from the convex parabolic distribution (Fig. 2A) that is known from PB theory and the real-valued solutions regime of [30]. In the shaded part of Fig. 2, particle density is symmetrical and highest directly near the charged surfaces, but zero in the middle. Keeping a constant surface charge and increasing separation d, the particle distribution starts to change; concentration at the charged surfaces decreases as we approach the limit of maximum separation (Fig. 2B and C) until in the extreme case it falls off to zero at the surfaces. The highest density is localized in two symmetrical peaks from each charged surface (Fig. 2C). We could by analogy fix the distance d and begin increasing σ. This would correspond to moving along the σ axis.

Particle distributions would again change from normal parabolic distributions (Fig. 2A) to two-peak ones (Fig. 2C). Since k depends both on d and σ, every point in the shaded region of Fig. 2 corresponds to a different number density distribution.

4.2 Helmholtz free energy

Normalized Helmholtz free energy evaluation of the system at given values of d and σ is calculated as the integral

$$f(d,\sigma) = f_0 \int_0^1 \left(\alpha n^{5/3}(x) + E^2(x)\right) dx. \tag{48}$$

Here, f_0 is the area energy density of a classical plate capacitor given by $f_0 = \sigma^2 d/2\varepsilon_0$. Considering Fig. 2, we see there are two approaches to calculating the energy density:

- at separation d and corresponding limit of surface charge $\sigma_{\max}(d)$. This corresponds to energy along the line that separates the shaded and unshaded area of Fig. 2. We label this extreme value of energy density $f_{\sigma_{\max}}$;
- at separations $d \in (d_{\min}, d_{\max})$ at constant surface charge $\sigma_{\max}(d_{\max})$. For all calculations we set $d_{\min} = 0.01$ nm. This corresponds to energies calculated in the shaded part of Fig. 2 along lines of constant surface charge.

Fig. 3 shows dependencies of the Helmholtz free energy on surface separation. Looking at the extreme regime of $f\sigma_{\max}$ (Fig. 3A), we see that the energy density is a monotonous function that for two orders of magnitude in surface separation spans many orders of magnitude of free energy values. The exponential dependence occurs as a consequence of Eq. (47) and on the fact that electrostatic energy of the system F_{el} is dependent on surface charge density (see [30]). In the constant surface charge regime, the Helmholtz free energy density is a monotonously decreasing function when surface separation is increased, but reaches a local minimum at $d \approx 0.90$ nm before slightly increasing again (Fig. 3B). This is true if we use $\sigma_{\max}(d = 1\,\text{nm}) \approx 0.006\ \text{C/m}^2$. Had we used a different value of surface charge $\sigma_{\max}$, for example, $\sigma_{\max}(d = 2\,\text{nm})$ or $\sigma_{\max}(d = 3\,\text{nm})$ we would obtain the energy minimum at the same relative, and corresponding, values of surface separation, that is at $d \approx 1.80$ nm and $d \approx 2.70$ nm, respectively. In all cases, the ratio of the minimum energy position to surface separation at respective $\sigma_{\max}(d_0)$ is

$$d_{\text{MIN}}/d_0 = 0.90, \tag{49}$$

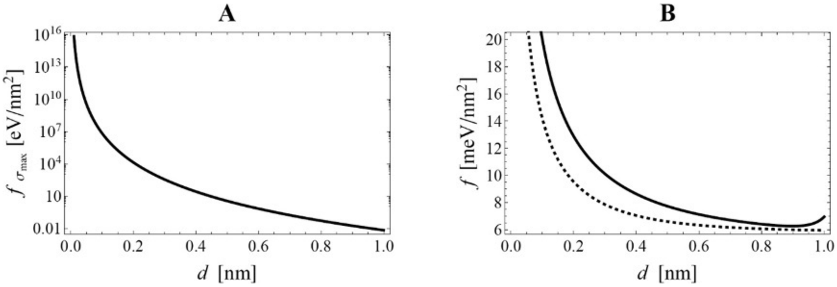

Fig. 3 Helmholtz free energy of the system vs. surfaces separation. (A): Free energy density at extreme values of σ_{max}, where solutions are still physically relevant. (B): Free energy density at constant value of σ_{max}(1 nm) 0.006 C/m^2 at varying distance between the surfaces. The full line uses the complex solution, while the dashed line is the real-valued solution in the low-temperature limit [30]. Note the slight increase in energy at $d = 0.90$.

where d_{MIN} is the distance of Helmholtz energy minimum and d_0 is the surface separation (and corresponding σ_{max}) at which energy is calculated. The energy density values at these local extrema are different, but the minima always occur at the same relative surface separation (Fig. 4). This fact is expected as our governing equation (Eq. 13) is merely dependent on one parameter (β). At every surface separation and corresponding σ_{max} the dimensionless electric field, electric potential and particle number density are identical, as the quantities stay congruent. Only after considering the units of measurement do they diverge in their absolute values, as seen in Fig. 4.

In Fig. 4, Helmholtz free energy was calculated using the σ_{max} for a specified distance between the surfaces d. We see that this value always occurs at d_{MIN} between the surfaces. For $d_0 = 1$ nm, the Helmholtz energy value in the minimum is 6.26 meV/nm^2, for $d_0 = 2$ nm, this is 12.22 μeV/nm^2 and for $d_0 = 3$ nm, this is 0.32 μeV/nm^2. No matter what the distance between the surfaces is, the minimum always occurs at the same relative distance d_{MIN}, which implies that the same dimensionless energy density is obtained for a chosen value of d and its corresponding σ_{max}. The potential and number density spatial dependencies look identical at that chosen set of parameters. The Helmholtz free energy density of the complex solution at every model parameter (β) always results in a relatively larger value over its real-valued counterpart, which we interpret as a thermodynamically less favorable solution (Fig. 3B). Electric potential, electric field and particle density of real-valued solutions are compared to complex solutions in Fig. 5.

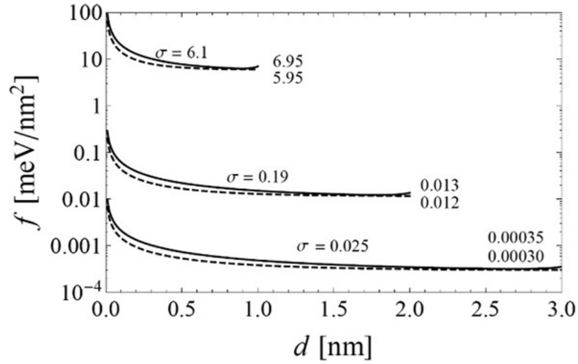

Fig. 4 A logarithmic plot of Helmholtz free energy for three distinct values of surface separation *d*. The dashed line denotes the real solution at identical parameters for comparison while the numbers show the energy density at extreme values of 1, 2, and 3 nm; the top number for the complex solution and the bottom number for the real solution. The surface charge density at which the plots were calculated is in units mC/m^2.

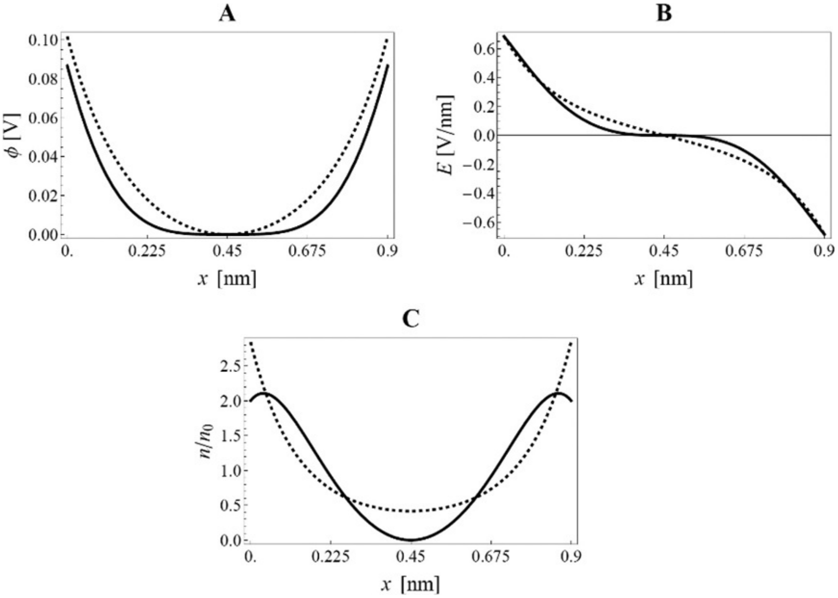

Fig. 5 At minimum energy, the dependence of (A) potential, (B) the electric field and (C) particle number density. Full line: complex, dashed line: numerical real solution taken from Ref. [30].

In the scope of our investigations, both curves never intersected with each other. The minimum of the energy perhaps points to a possible metastable state solution of electron configurations. Since our model offers no insight into electron distribution other than number density of particles at each coordinate x, the nature of these metastable solutions remains beyond the scope of the presented results.

4.3 Attractive force between charged plates

The force between the charged surfaces s per unit area is defined as the spatial derivative of Helmholtz free energy per unit area, in our case only in the x-dimension

$$s = -\nabla f, \qquad s_x = -\frac{\partial f}{\partial d}. \tag{50}$$

Since we observe a minimum in free energy, we expect that at a constant surface charge $\sigma_{\max}$ and changing distance between the surfaces, the force per unit area between them will not be monotonous. This can be seen in Fig. 6.

It is known that like-charged surfaces are commonly attracted to each other in the presence of multivalent counterions [23–25] and spherical particles with a quadrupolar charge distribution [26]. Poisson-Boltzmann theory of point-like particles is a first-order approximation for weak electric fields and low particle concentrations, so attraction between two charged surfaces is never predicted. It has however been reported that point-like particles can induce attraction for high coupling constants (pertaining to a high degree of strength of interaction between counterions and charged surfaces), as shown by Monte-Carlo simulations [27]. We may draw an analogy to this strong ion-surface coupling by observing that in our model surface attraction happens only in vicinity of $\sigma_{\max}$ for every d. In other words, strong coupling—and consequential attraction of surfaces—is only possible at high values of σ.

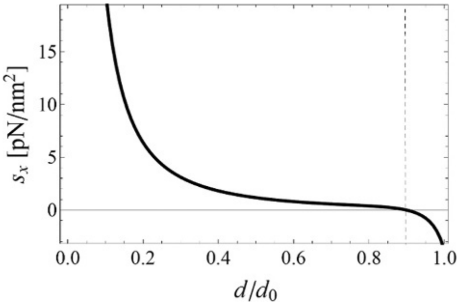

Fig. 6 The force between charged surfaces per unit area s_x in dependence on distance of separation d. Here, $d_0 = 1$ nm and $\sigma = 0.006$ C/m^2.

4.4 Differential capacitance

Differential capacitance is a quantity of importance in energy storing properties of capacitors. It is defined as

$$C = \frac{d\sigma}{d\phi(x=0)}. \tag{51}$$

The first step in the derivation is finding the dependence $\phi(x = 0)$. We can easily obtain this by inserting $x = 0$ into Eq. (40). We get

$$\phi(x=0) = \frac{1 - \cos\left(\frac{k}{2}\right)\cosh\left(\frac{k}{2}\right)}{k\left(\cosh\left(\frac{k}{2}\right)\sin\left(\frac{k}{2}\right) - \cos\left(\frac{k}{2}\right)\sinh\left(\frac{k}{2}\right)\right)}. \tag{52}$$

Using Eqs. (34)–(37) we may express the parameter k merely by the distance between charged surfaces d and surface charge density σ:

$$k = \frac{2^{21/8}}{K^{9/8}\sqrt{5}}\left(\frac{\pi}{3}\right)^{3/4} d^{15/8}\sigma^{3/8} = \Lambda d^{15/8}\sigma^{3/8}. \tag{53}$$

The numerical constant Λ is equal to

$$\Lambda = 3{,}20 \cdot 10^{18}. \tag{54}$$

Remembering that until now most of our results were in dimensionless, reduced units, we must consider the potential in units of volts since the normalization was made with the parameter d involved,

$$\phi = \phi_0\widetilde{\phi}, \qquad \phi_0 = \frac{d\sigma}{\varepsilon_0}. \tag{55}$$

The dependence of the electric potential at the surfaces $\phi(x=0)$ in units of volts is thus given by

$$\phi(x=0)(d,\sigma) = \frac{\sqrt{5}}{2^{21/8}}\left(\frac{3}{\pi}\right)^{3/4}\frac{\sigma^{5/8}}{d^{7/8}\varepsilon_0}\,\frac{\left(1 - \cos\left(\frac{\Lambda\xi}{2}\right)\cosh\left(\frac{\Lambda\xi}{2}\right)\right)}{\left(\cosh\left(\frac{\Lambda\xi}{2}\right)\sin\left(\frac{\Lambda\xi}{2}\right) - \cos\left(\frac{\Lambda\xi}{2}\right)\sinh\left(\frac{\Lambda\xi}{2}\right)\right)}, \tag{56}$$

where

$$\xi = d^{15/8}\sigma^{3/8}. \tag{57}$$

If we set the value of d to $d = 10^{-9}$ and implicitly differentiate by $d/d\phi(x=0)$, we arrive at differential capacity $d\sigma/d\phi(x=0)$. Numerically this

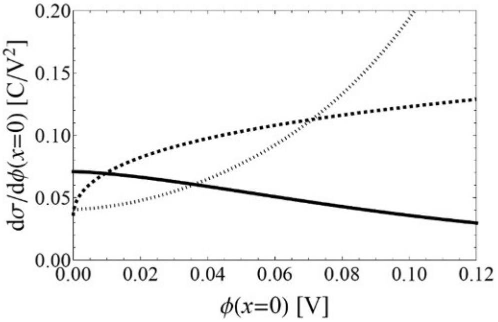

Fig. 7 Differential capacity of the model capacitor at $d=1$ nm for the complex solution (full line), the real low-temperature limit solution (dashed line) and the real high-temperature limit (dotted line) at $T=300$ K. The real-valued solutions were taken from Ref. [30].

is done by calculating a table of values $\phi(x=0)(\sigma)$ in range up to $\sigma_{\max}(d=10^{-9})$, inversing the function and differentiating its fit. We see the differential capacity in Fig. 7. In comparison to real-valued solutions, differential capacitance is a decreasing function of surface potential $\phi(x=0)$, but stays similar within the order of magnitude. For comparison, the high-temperature limit of classic Boltzmann distributions is also shown.

5. Conclusions

Building upon our previous work considering the quantum effects in the EDL [30], we found a new set of solutions of electric potential and particle number density pertaining to a global thermodynamic equilibrium. These solutions predicted a diffuse particle distribution between the charged surfaces. We found that the Helmholtz free energy dependence is not always a monotonous decreasing function of surface separation, implying that Fermi-Dirac statistics restrictions mediate attractive force between the charged surfaces at certain parameters of the system. The new solution predicted a differential capacitance of the system that qualitatively differs from corresponding previous results [30] as well as from the results of the Poisson-Boltzmann theory. These results may be significant in biological systems where processes at small scales could be an important driving factor of energy storage and surface adhesion effects between membranes.

Acknowledgments

This research was funded by the Slovenian Research Agency (ARRS), grant numbers P2-0232, L3-2621, J3-3074, J3-3066 and J3-2533.

Conflict of interest

The authors declare no conflicts of interest in this paper.

References

[1] A. Miodek, et al., Electrochemical aptasensor of human cellular prion based on multiwalled carbon nanotubes modified with dendrimers: a platform for connecting redox markers and aptamers, Anal. Chem. 85 (16) (2013) 7704–7712.

[2] P. Kowalczyk, et al., Effects of critical fluctuations on adsorption-induced deformation of microporous carbons, J. Phys. Chem. C 119 (11) (2015) 6111–6120.

[3] R. Imani, et al., Band edge engineering of TiO 2@ DNA nanohybrids and implications for capacitive energy storage devices, Nanoscale 7 (23) (2015) 10438–10448.

[4] M. Kulkarni, et al., Wettability studies of topologically distinct titanium surfaces, Colloids Surf. B Biointerfaces 129 (2015) 47–53.

[5] R. Imani, et al., Multifunctional gadolinium-doped mesoporous TiO2 nanobeads: photoluminescence, enhanced spin relaxation, and reactive oxygen species photogeneration, beneficial for cancer diagnosis and treatment, Small 13 (20) (2017) 1700349.

[6] J. Manzanares, S. Mafé, J. Bisquert, Electric double layer at the membrane/solution interface: distribution of electric potential and estimation of the charge stored, Ber. Bunsen. Phys. Chem 96 (4) (1992) 538–544.

[7] I. Bivas, Electrostatic and mechanical properties of a flat lipid bilayer containing ionic lipids: possibility for formation of domains with different surface charges, Colloids Surf. A Physicochem. Eng. Asp. 282 (2006) 423–434.

[8] X. Chen, et al., Electrical nanogap devices for biosensing, Mater. Today 13 (11) (2010) 28–41.

[9] R.D. Munje, et al., Flexible nanoporous tunable electrical double layer biosensors for sweat diagnostics, Sci. Rep. 5 (1) (2015) 1–11.

[10] R. Srivastava, The role of proton transfer on mutations, Front. Chem. 7 (2019) 536.

[11] S. McLaughlin, The electrostatic properties of membranes, Annu. Rev. Biophys. Biophys. Chem. 18 (1) (1989) 113–136.

[12] M. Gouy, Sur la constitution de la charge électrique à la surface d'un électrolyte, J. Phys. Theor. Appl. 9 (1) (1910) 457–468.

[13] D.L. Chapman, LI. A contribution to the theory of electrocapillarity, Lond. Edinb. Dublin Philos. Mag. J. Sci. 25 (148) (1913) 475–481.

[14] R. Parsons, The electrical double layer: recent experimental and theoretical developments, Chem. Rev. 90 (5) (1990) 813–826.

[15] O. Stern, Zur theorie der elektrolytischen doppelschicht, Z. Elektrochem. Angew. Phys. Chem. 30 (21–22) (1924) 508–516.

[16] V. Kralj-Iglič, A. Iglič, A simple statistical mechanical approach to the free energy of the electric double layer including the excluded volume effect, J. Phys. II 6 (4) (1996) 477–491.

[17] I. Borukhov, D. Andelman, H. Orland, Steric effects in electrolytes: a modified Poisson-Boltzmann equation, Phys. Rev. Lett. 79 (3) (1997) 435.

[18] A. Velikonja, V. Kralj-Iglič, A. Iglič, On asymmetric shape of electric double layer capacitance curve, Int. J. Electrochem. Sci 10 (1) (2015) 1–7.

[19] J. Bikerman, XXXIX. Structure and capacity of electrical double layer, Lond. Edinb. Dublin Philos. Mag. J. Sci. 33 (220) (1942) 384–397.

[20] E. Gongadze, et al., Langevin Poisson-Boltzmann equation: point-like ions and water dipoles near a charged surface, Gen. Physiol. Biophys. 30 (2) (2011) 130.

[21] E. Gongadze, A. Iglič, Asymmetric size of ions and orientational ordering of water dipoles in electric double layer model-an analytical mean-field approach, Electrochim. Acta 178 (2015) 541–545.
[22] T.L. Hill, An Introduction to Statistical Thermodynamics, Courier Corporation, 1986.
[23] N. Ise, T. Konishi, B. Tata, How homogeneous are "homogeneous dispersions"? Counterion-mediated attraction between like-charged species, Langmuir 15 (12) (1999) 4176–4184.
[24] Y. Levin, Electrostatic correlations: from plasma to biology, Rep. Prog. Phys. 65 (11) (2002) 1577.
[25] K. Besteman, et al., Direct observation of charge inversion by multivalent ions as a universal electrostatic phenomenon, Phys. Rev. Lett. 93 (17) (2004), 170802.
[26] J. Urbanija, et al., Attraction between negatively charged surfaces mediated by spherical counterions with quadrupolar charge distribution, J. Chem. Phys. 129 (10) (2008) 09B609.
[27] J. Zelko, et al., Effects of counterion size on the attraction between similarly charged surfaces, J. Chem. Phys. 133 (20) (2010), 204901.
[28] K. Bohinc, et al., Attraction of like-charged surfaces mediated by spheroidal nanoparticles with spatially distributed electric charge: theory and simulation, Adv. Planar Lipid Bilayers Liposomes 9 (2009) 279–301.
[29] N. Lang, W. Kohn, Theory of metal surfaces: charge density and surface energy, Phys. Rev. B 1 (12) (1970) 4555.
[30] M. Drab, V. Kralj-Iglič, Diffuse electric double layer in planar nanostructures due to Fermi-Dirac statistics, Electrochim. Acta 204 (2016) 154–159.
[31] M. Drab, V. Kralj-Iglič, Electric double layer of electrons: attraction between two like-charged surfaces induced by Fermi–Dirac statistics, Phys. Lett. A 383 (4) (2019) 358–365.

Serial Editors

Aleš Iglič,
University of Ljubljana, Slovenia

Michael Rappolt
University of Leeds, UK

Patricia Losada-Pérez
Université Libre de Bruxelles, Belgium

Cover image: Optical micrographs of butter (a, b) and butter oil (c-e). In panel (f) a SEM image of brown residue is shown (before hexane wash). Scale bar in all images indicate 100 µm

ISBN 978-0-323-98596-3

9 780323 985963

ELSEVIER

ACADEMIC PRESS
An imprint of Elsevier
elsevier.com/books-and-journals